Chapter 6
X-Ray CT Scanners and Application Examples

The various devices and technical components that compose an X-ray CT scanner were comprehensively discussed in Chap. 4. Furthermore, applied technologies conducted with industrial X-ray CT scanners were discussed in Chap. 5. It is likely exceptionally rare that standard users of X-ray CT scanners would examine and select the various constituent devices upon understanding the various technical components of X-ray tomography and assemble an industrial X-ray CT scanner by themselves. Instead, users are more likely to select commercially available X-ray CT scanners and introduce them to their affiliated institution, contract measurements to public research institutions (e.g. universities) or private measurement contractors, or rent the devices from these institutions.

Commercially available X-ray CT scanners are rapidly advancing, and higher-performance/higher-functionality products are released almost every year. As such, it may appear that providing an overview of the specifications of commercially available X-ray CT scanners may not be appropriate for a technical book that focuses on fundamental technologies as presented here. However, X-ray CT scanner performance cannot be entirely discussed with just the various constituent devices and technical components discussed in Chap. 4. In other words, the methods in which the various component technologies that were not fully discussed in Chaps. 4 and 5 are combined and the techniques that have integrated the various component technologies, careful consideration and innovations, and advanced user-friendly software more often than not stipulate the strengths, versatility, and characteristic applications of the X-ray CT scanner system. Therefore, with the understanding that this book will inevitably become obsolete, the present chapter introduces the latest X-ray CT scanners that are commercially available at the time that this book was written, as well as superior examples of their application. These X-ray CT scanners may appear somewhat outdated with time. However, the technologies and innovations incorporated in these scanners will certainly be effectively applied in subsequent X-ray CT scanners or future developments will be based on them.

H. Toda, *X-Ray CT*,
https://doi.org/10.1007/978-981-16-0590-1_6

In writing this chapter, many of the manufacturers of these X-ray CT scanners were directly approached for information regarding the characteristics of the products from each company and their notable application examples. Support was also provided by the radiation department (department head at the time of writing this book: Masahito Natsuhara, Shimadzu Co.) of the Japanese Inspection Instrument Manufacturers' Association (JIMA), a business group of nondestructive inspection instrument manufacturers in Japan.

6.1 General-Use X-Ray CT Scanners for Industrial Use

Table 6.1 displays specifications of representative industrial X-ray CT scanners. Photographs of industrial X-ray CT scanners with high versatility among the scanners listed in Table 6.1 are shown in Fig. 6.1. Manufacturers have provided detailed specifications, which are normally not included even in catalogs, for this book. Combined with the descriptions of the various constituent devices shown in Chap. 4, we can develop a deeper understanding of industrial X-ray CT scanners.

The 14 types listed in Table 6.1 cover the representative tube voltage range of industrial X-ray CT scanners that use X-ray tubes. Many of these use tungsten as a reflection-type target. However, the cooling methods for tubes vary according to their output. Air-cooling is sufficient for low-output radiation sources but water-cooling and oil-cooling become necessary with higher output. Furthermore, X-ray tubes include sealed and open variations. The open type allows for filaments to be exchanged when they are broken, but the sealed type needs to have the entire tube replaced. In recent years, some manufacturers have provided maintenance services in which the sealed tube is temporarily collected, the filament exchanged, and the tube returned. Materials with a small atomic number (e.g. beryllium) are often used for the radiation window of the X-ray source and the window material can avoid issues caused by the absorption of low-energy X-rays. Furthermore, aluminum is frequently used as a window material for devices that require high-energy X-rays.

Figure 6.2 is a visualization example of fiber-reinforced plastic (FRP) using the X-ray CT scanner (Shimadzu Co. inspeXio SMX225CT FPD HR) shown in Table 6.1 with a tube voltage of 225 kV. This X-ray CT scanner is equipped with a large-scale, high-resolution flat-panel detector (corresponding to 14 million pixels). The tube voltage is relatively high at 225 kV, but low-energy X-rays can be used due to the specialized carbon plate used in the radiation window of the X-ray source. This enables the clear visualization of carbon fiber- or glass fiber-reinforced plastic composites (CFRP and GFRP, respectively) or non-woven fibers. This also is due to the high dynamic range of the incorporated flat panel detector. Comparisons of Fig. 6.2a and b show how much the dynamic range difference (14 bit vs. 16 bit) in a detector plays a role in image quality. These types of fiber orientation measurements in CFRP or GFRP can be easily conducted with optional software. Figure 6.2b is an example of a carbon fiber-reinforced thermoplastic (CFRTP). Industrial X-ray CT scanners can provide a measurement technology environment, which controls the

Table 6.1 Detailed specifications of representative X-ray CT scanners

Manufacturer		SHIMADZU		NIKON		OMRON
Type		inspeXio SMX-90CT Plus	inspeXio SMX225CT FPD HR	XT H 225 ST	XT H 450	VT-X750
X-ray source	Type	Sealed tube	Open tube	Open tube	Open tube	Sealed tube
	Output (W)	−10	−135	225	450	−39
	Tube voltage (kV)	−90	−225	225	450	−130
	Tube current (mA)	0.11	0.6	0–2	0–2	−0.3
	Focal spot size (μm)	5	−4	3	80	
	Maximum beam diameter (μm)	–	7	–	–	–
	Target material	Tungsten	Tungsten	Tungsten, etc	Tungsten	Tungsten
	Target type	Reflective target	Reflective target (cylindrical)	Reflective target	Reflective target	–
	Target angle (°)	45	45	–	–	–
	Emission angle (°)	40	40	–	–	45
	Filter	Various materials	Various materials	Cu, etc	Cu	Various materials
	Window material	Be	Special carbon	Be	Al	Be
	Tube cooling system	Air cooling	Water cooling	Water cooling	Oil cooling	Air cooling

(continued)

Table 6.1 (continued)

Manufacturer		SHIMADZU		NIKON		OMRON
Type		inspeXio SMX-90CT Plus	inspeXio SMX225CT FPD HR	XT H 225 ST	XT H 450	VT-X750
Stage	Load bearing capacity (kg)	2	12	50	100	4 (Transportation conveyor)
	Inclination of a rotation axis	No	Possible (optional)	Possible	No	No
Detector	Type	FPD	FPD	FPD	FPD/CLDA	FPD
	Scintillator	CMOS	Amorphous	–	–	–
	Number of pixels	1000 × 1000	3000 × 3000	2000 × 2000/4000 × 4000	2000 × 2000/4000 × 4000	–
	Pixel size (μm)	50 × 50	139 × 139	200/100	200/100/400	–
	Dynamic range	12 bit	16 bit	–	–	14 bit
Total	Max. spatial resolution (μm)	10	4	–	–	6/pixel
	Offset scan	Possible	Possible	–	–	No
	Volume rendering software	Attached	Attached	–	–	Attached
	Image analysis software	VGStudio	VGStudio	VGStudio	VGStudio	Attached
	Dimensions (mm)	830 × 601 × 587	2170 × 1350 × 1857	2414 × 1275 × 2202	3616 × 1828 × 2249	1550 × 1925 × 1645
	Weight (kg)	250	3100	4200	14,000	2970

(continued)

Table 6.1 (continued)

RX SOLUTIONS		ZEISS		Hitachi	
DeskTom130	EasyTom150	ZEISS Xradia 810 Ultra	ZEISS Xradia 520 Versa	HiXCT-1 M	HiXCT-9 M
Sealed tube	Sealed tube	Open tube	Sealed tube	Compact linear accelerator	Compact linear accelerator
−40	−75	875	10	–	–
−130	−150	35 (Effective value: 5.4 keV)	160	950	9000
−0.3	−0.5	25	0.075	–	–
5	5	75	–	2000	1600
–	–	75	–	–	–
Tungsten	Tungsten	Chromium	Tungsten	Tungsten	Tungsten
Reflective target	Reflective target	Rotating anode	Transmissive target	Transmissive target	Transmissive target
–	–	–	0	–	–
–	–	–	–	45	30
Various materials	Various materials	–	Various materials	No	No
Be	Be	Be	Diamond	–	–
Air cooling	Air cooling	Water cooling	Air cooling	Air cooling	Water cooling
2	30	1	25	100	100
Possible (optional)	Possible (optional)	–	–	–	–
FPD	FPD	FZP + optical lens + CCD	Optical lens + CCD (FPD)	Line sensor	Line sensor
CsI or Gadox	CsI or Gadox	– (Patented technology)	– (Patented technology)	Si semiconductor	Si semiconductor
1920 × 1536	1920 × 1536	1024 × 1024	2048 × 2048 (CCD)	750–	750–
127 × 127	127 × 127	–	–	–	–

(continued)

Table 6.1 (continued)

RX SOLUTIONS		ZEISS		Hitachi	
DeskTom130	EasyTom150	ZEISS Xradia 810 Ultra	ZEISS Xradia 520 Versa	HiXCT-1 M	HiXCT-9 M
16 bit	16 bit	16 bit	16 bit	16 bit	16 bit
4	5	0.05	0.7	200	200
Possible	Possible	–	Possible	Possible	Possible
Attached	Attached	Attached	Attached	–	–
VGStudio, VGStudioMAX	VGStudio, VGStudioMAX	ORS Dragonfly Pro (optional)	ORS Dragonfly Pro (optional)	VGStudio	VGStudio
1250 × 800 × 1800	2100 × 1100 × 2000	2180 × 1200 × 2170	2170 × 1190 × 2090	830 × 601 × 587	6000 × 6000 × 6000
700	2000	2600	2468	60,000–80,000 with radiation shielding	15,000 without radiation shielding

JED	RF	Yamaha motor
CTH200 FPD	NAOMi-CT	YSi-X TypeHD
Sealed tube	Sealed tube	Sealed tube
−150	−500	−39
−200	50–100	−130
−0.75	2–10	−0.3
20	500	−16
–	–	−50
Tungsten	Tungsten	Tungsten
Reflective target	Reflective target	Reflective target
–	5	45
40	–	100

(continued)

Table 6.1 (continued)

JED	RF	Yamaha motor
Various materials	Cu	Various materials
Special glass	–	Be
Air cooling	Oil/air cooling	Air cooling
10	10	2 (Transportation conveyor)
No	No	No
FPD	FPD	FPD
Amorphous	CSI	–
1025 × 1025	1232 × 1216	–
200 × 200	100	–
16 bit	12 bit	14 bit
–	5 LP/mm	7
Possible	Possible	No
Attached	Attached	Attached
Attached	Attached	Attached
1550 × 1092 × 1413	623 × 338 × 297.5	1710 × 1883 × 1705
1860	50	2900

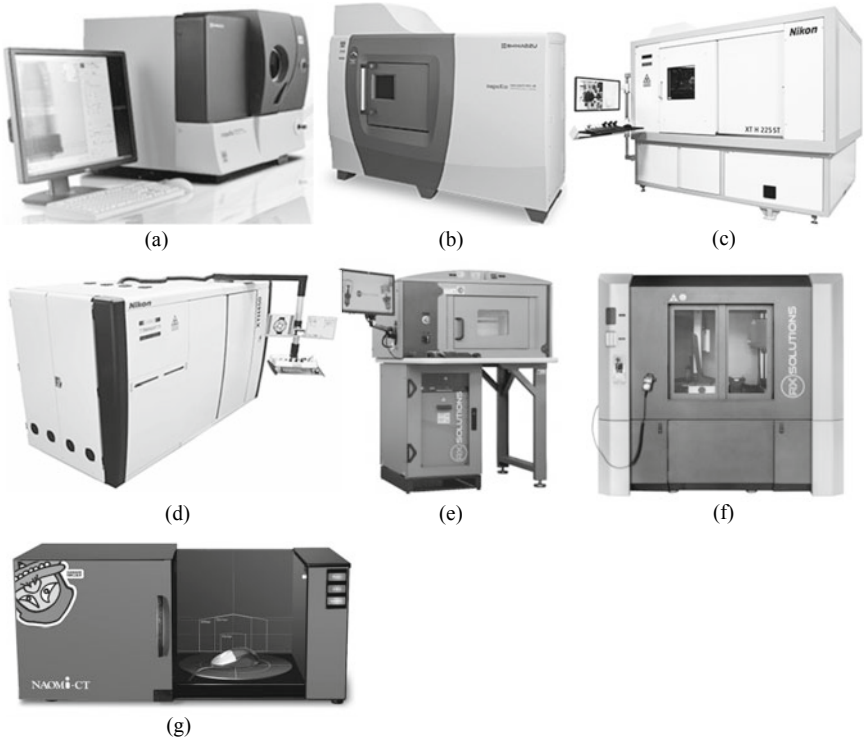

(a) (b) (c)

(d) (e) (f)

(g)

Fig. 6.1 Photographs of commercially available X-ray CT scanners described in Table 6.1; **a** Shimadzu Co. inspeXio SMX-90CT Plus model from Table 6.1 and **b** inspeXio SMX225CT FPD HR model (both courtesy of Masahito Natsuhara of Shimadzu Co.); **c** and **d** are the Nikon XT 225 ST model and XT H 450 model, respectively, from Table 6.1 (both courtesy of Satoshi Kazama of Nikon); and **e** and **f** are RX SOLUTIONS DeskTom 130 model and EasyTom 150 model from Table 6.1 (both courtesy of Wataru Adachi of Seikoh Giken). **g** RF Co. NAOMi-CT model (courtesy of Kazumi Kodaira of RF Co.)

important factor of fiber misalignment when handling CFRTP. As shown in Fig. 6.3, other applications of this X-ray CT scanner include the deformation analysis of lithium-ion batteries and high-spatial-resolution/high-contrast observations of separators. High spatial resolution and high contrast can be obtained in this way. Additionally, fast tomography with a maximum speed of 33 s/scan and fast image reconstruction in as fast as 5 s has become possible with detector improvements and software updates.

Figure 6.4 shows imaging conducted on pearls. This was conducted using the RX SOLUTIONS device (DeskTom130) shown in Table 6.1. A pearl is a light substance with inorganic materials like calcium carbonate and calcium oxide as its principal components. Figure 6.4 shows that the pearl core and pearl layers, as well as its boundary layers, were clearly visualized. We can observe that the pearl core/pearl layer and boundary layer, which have minimal compositional differences, are clearly

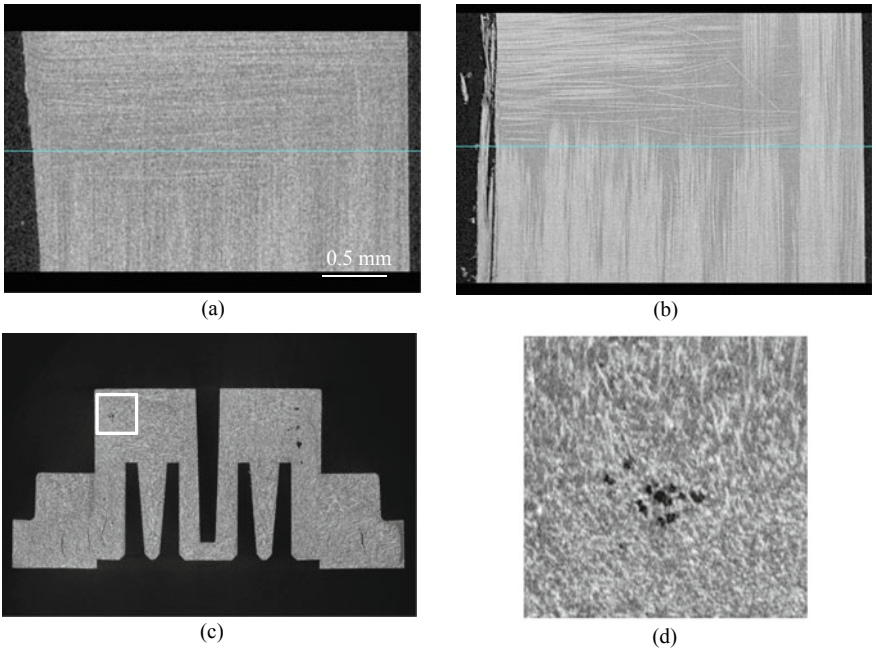

Fig. 6.2 **a** Cross-section image when visualizing CFRP using an X-ray CT scanner with a 14-bit flat panel detector; **b** is a visualization example using an X-ray CT scanner with a 16-bit flat panel detector described in Table 6.1 (Shimadzu Co. inspeXio SMX225CT FPD HR model); **c** visualization of GFRP using the same device; and **d** magnification of the enclosed area in **c** (both courtesy of Masahito Natsuhara of Shimadzu Co.)

distinguished. This visualization demonstrates how the boundary layer is broken and how this results in the deformation of the pearl surface.

Many X-ray CT scanners can handle imaging regions of interest that are considerably smaller than the sample diameter. This enables the local/high-magnification observation of large samples, which do not fit within the field of view within a detector, such as electric circuit boards. Figure 6.3 is one such observation example. Furthermore, Fig. 6.5 shows an observation of a soldered section of an electronic circuit board using the RX SOLUTIONS machine (DeskTom130) shown in Table 6.1. The existence of pores in the solder, which are likely to result in fracture, can be confirmed using the microfocus tube.

Many of the devices in Table 6.1 can handle offset scans. As described in Sect. 3.3.5 (1), offset scans can be used to magnify the sample size by integer multiples of the X-ray beam width. In this case, the included software can automatically stitch together multiple transmission images due to the high-accuracy offset. However, care must be taken concerning the penetrative power of the X-ray.

Incidentally, it can be observed from Table 6.1 that many X-ray CT scanners use a microfocus X-ray tube. The need for high spatial resolution is also firmly rooted in industrial X-ray CT scanners. There have been products that have two tubes with

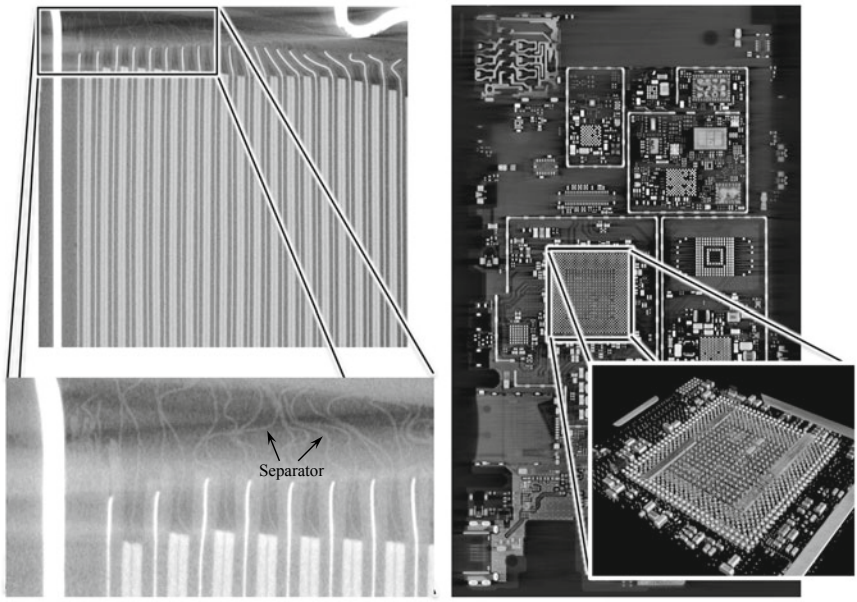

Fig. 6.3 **a** Example of a high-resolution/high-contrast observation of lithium ion battery deformation and the separators and **b** an observation of the electronic circuit board of a smartphone and a high-magnification observation of the enclosed CPU. Each are visualization examples using the same X-ray CT scanner (Shimadzu Co. inspeXio SMX225CT FPD HR model) from Fig. 6.2 (courtesy of Masahito Natsuhara from Shimadzu Co.)

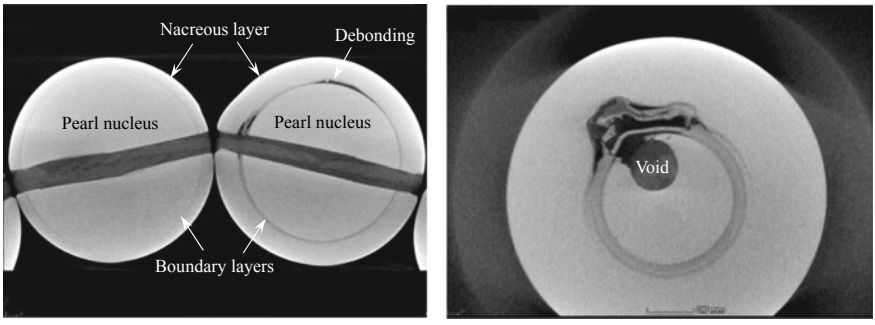

Fig. 6.4 Interior structure of a pearl observed using an RX SOLUTIONS device (DeskTom130) in Table 6.1. The pearl on the right in **a** and the pearl in **b** show damaged boundary layers between the pearl core and pearl layers (courtesy of Wataru Adachi from Seikoh Giken)

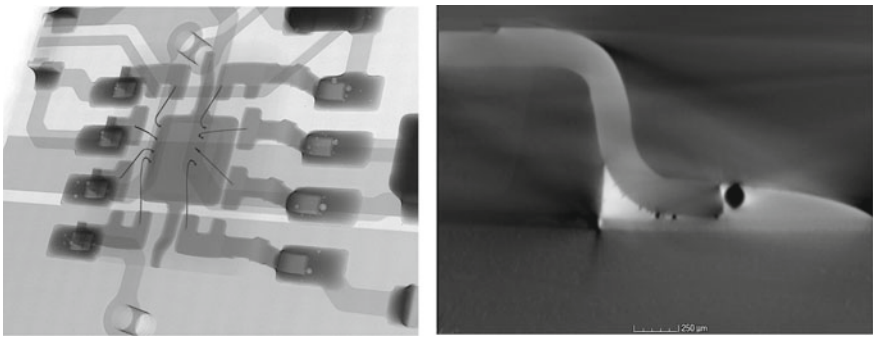

(a) (b)

Fig. 6.5 **a** Transmission image of an electronic circuit board after the completion of soldering; **b** is a virtual cross-section observed from the side in a 3D image of a soldering section. The device used is the RX SOLUTIONS DeskTom130 model shown in Table 6.1 (courtesy of Wataru Adachi of Seikoh Giken)

varying focal spot size/output values installed, also referred to as multifocus. Its applications are innumerable, from the currently-expanding field of layered manufacturing to assessment of the aforementioned CFRP and GFRP fiber orientation, to various assessments in archaeology. For example, high-spatial-resolution imaging with low-energy X-rays in the archaeological disciplines can be used to determine whether an ancient tree was a coniferous or broadleaf tree and can even be used to analyze what the tree species was. The focal spot size of X-ray tubes and maximum spatial resolution of X-ray CT scanners are shown in Table 6.1. Their current state is such that the former is generally used as an index for spatial resolution. However, it must be noted that the focal spot size of X-ray tubes is but one of the factors that regulate the spatial resolution of X-ray CT scanners. Data provided directly from the manufacturer are shown here, and there is no follow-up on how the maximum spatial resolution of the device is measured or assessed. Those who have read this book would likely understand what spatial resolution is and how this is measured. It is recommended that the cross-sectional images of a sample that approximates the desired 3D image and imaging conditions be obtained and evaluated independently.

Figure 6.6 shows an observation example of an archaeological artifact excavated from the ancient ruins of Antikythera in Greece using an X-ray CT scanner (Nikon XT H 450 model) with a 450 kV tube voltage that enables the use of X-rays with high energies even among those in Table 6.1. This device is unique in that it is capable of having an X-ray tube with a relatively small focal point size despite having a tube voltage of 450 kV. For this reason, a high spatial resolution is achieved despite the high X-ray energy and output, where a maximum spatial resolution of approximately 200 μm is achieved. Usage of this X-ray CT scanner has enabled the visualizations of detailed patterns that were buried under rust on the surface of relatively large artifacts. These observations clarified that this archaeological artifact with a previously-unknown use was the world's oldest astronomical calendar. This

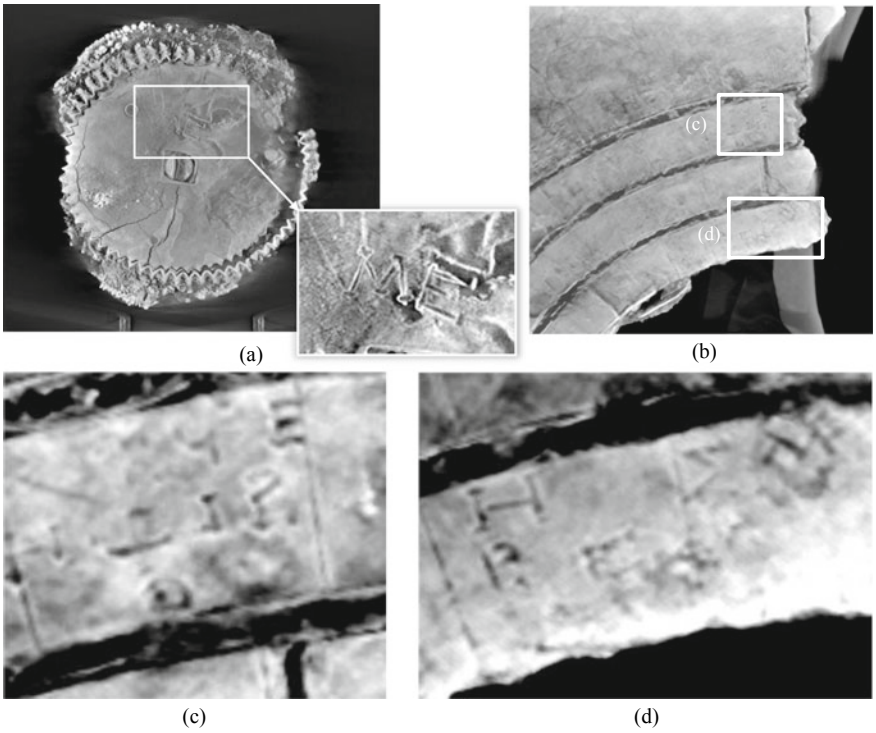

Fig. 6.6 **a** Full view of the excavated artifact from the ancient ruins of Antikythera in Greece; **b** shows a section of this; **c** and **d** are further magnifications of the section in (**b**); and (**c**) and (**d**) show patterns that indicate that this artifact was a calendar. These were visualized using a 450 kV tube voltage X-ray CT scanner (Nikon XT H 450 model) described in Table 6.1 (courtesy of Satoshi Kazama of Nikon)

is considered a good example of how industrial X-ray CT has provided valuable academic contributions.

Figure 6.7 shows an application example of an X-ray CT scanner with a slightly smaller tube voltage of 300 kV. This device has a microfocus tube whose distance between the X-ray focal spot and X-ray irradiation window is shorter at roughly 5 mm and whose automatic changes in focal spot dimensions, as per the cathode power of the X-ray tube, achieve a balance between X-ray penetrative power and relatively high spatial resolution. Figure 6.7 shows 3D images of gray cast iron and ductile cast iron materials where a specimen measuring □ approximately 2 mm was extracted. The graphite portions of each of the materials are extracted and displayed here. The thin and long flaky graphite is visualized with sufficient spatial resolution.

Many of the devices in Table 6.1 can handle inclinations in the sample rotation stage. This enables the implementation of the laminography discussed in Sect. 3.3.5 (3). In practice, many X-ray CT scanners with software that can handle laminography are commercially available, enabling imaging of plate-like samples that do not fit

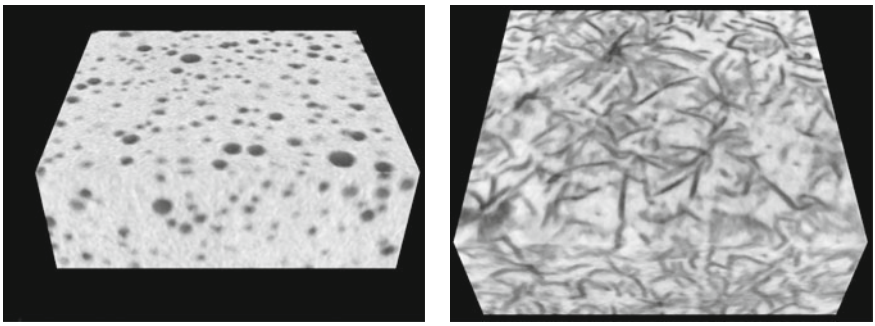

(a) (b)

Fig. 6.7 Graphite extracted from **a** spherical graphite cast iron and **b** flaky graphite cast iron. The microscale flaky graphite is visible. A 300 kV tube voltage X-ray CT scanner (Toshiba IT & Control Systems TOSCANER-33000μFD-ZII model) was used for observation (courtesy of Junichi Iwasawa of Toshiba IT & Control Systems)

within the X-ray beam range in standard imaging methods, such as electronic circuit boards, aluminum or steel body panels for automobiles, and fiber metal laminate thin plates for airplanes.

As shown in the detector row in Table 6.1, many products use a flat-panel detector. Image intensifiers typically offer the advantages of relatively low cost, high efficiency, and a high frame rate. However, flat-panel detectors have the advantages of a high dynamic range, few distortions such as with image intensifiers, and a large effective field of view. Combined with recent price reductions, flat-panel detectors are increasingly used. Furthermore, the 450-kV tube voltage device (Nikon XT H 450 model) in Table 6.1 also has a model with a line sensor camera. As discussed in Sect. 4.4.2 (1), the X-ray beam is formed into a fan beam using the collimator when using the line sensor camera to have the X-ray illuminate the sample only within the field-of-view of the line sensor camera. Forward scattering of high-energy X-rays in the case of a parallel beam or cone beam results in the emission of scattered X-rays into the detector pixel from the whole sample; this reduces contrast and spatial resolution. The use of a fan beam can effectively prevent this.

Figure 6.8 is a schematic that shows how image quality changes when either a line sensor camera or flat-panel detector is used. Imaging with a line sensor camera requires vertical scanning of the sample across 500–2000 layers; consequently, the imaging time necessarily becomes longer. However, the influence of scattering X-rays coming from the sample regions in the vertical directions is no longer present and high-quality images with low noise levels can be obtained. However, the scattered X-rays coming from adjacent regions in the longitudinal direction of the line sensor cannot be avoided, therefore, adjustments in the sample-detector interval are necessary.

Figure 6.9 shows an observation example of an aluminum die-casting cylinder block using a line sensor camera. X-ray scattering at high X-ray energies from cone beam-type X-ray CT scanners can make the linear profile sections swollen in a

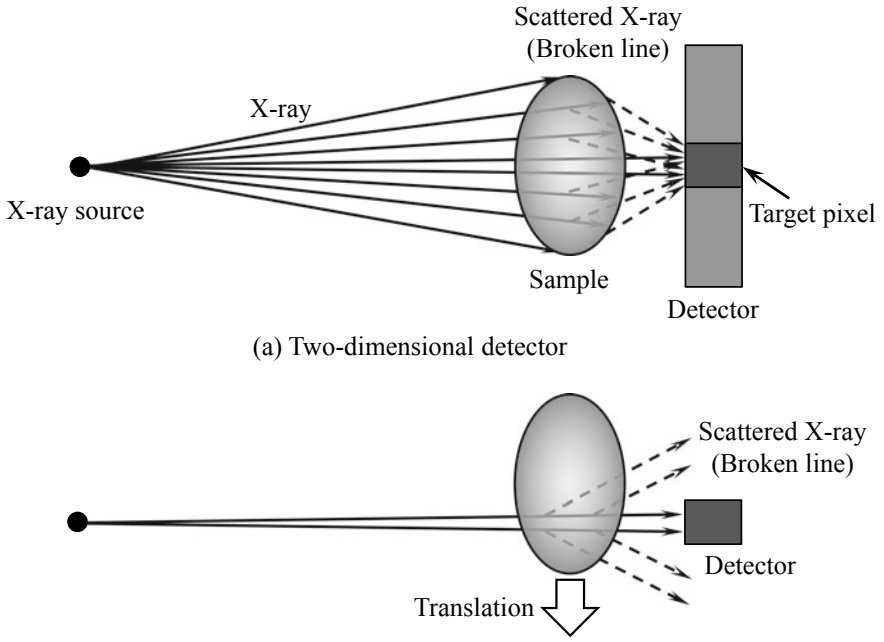

Fig. 6.8 Schematic showing differences in image quality between a line sensor camera device and a two-dimensional detector device (e.g. flat panel detector) when imaging with high-energy X-rays

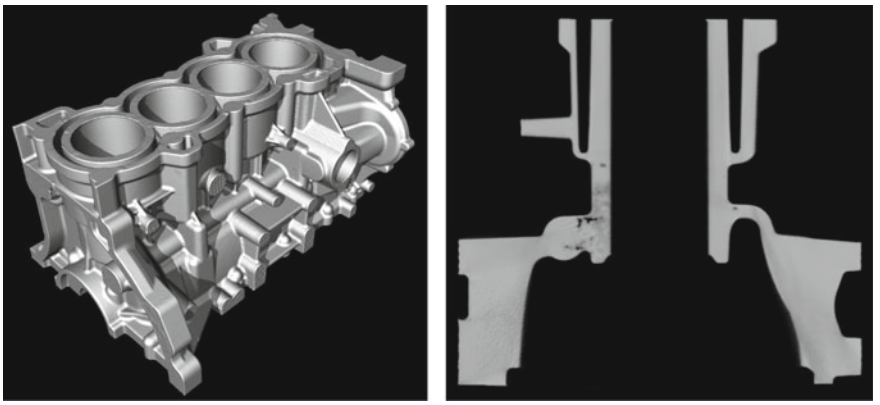

Fig. 6.9 Visualization example of an aluminum die-casting cylinder block; **a** is the total image and **b** is a virtual cross-section, which visualizes manufacturing defects such as internal cavities. A 450 kV tube voltage X-ray CT scanner (Toshiba IT & Control Systems TOSCNANER-24500twin model) was used for observations (courtesy of Junichi Iwasawa of Toshiba IT & Control Systems)

barrel-like shape. Line sensor cameras can ensure that geometrically accurate 3D images with no distortion can be obtained. Two rows of line sensor cameras are set up in the X-ray CT scanner and a third cross-section image can also be measured by supplementing the space between these two rows. Furthermore, increasing the scintillator thickness used for the line sensor camera can enable the acquisition of approximately 300 mm of transmission for aluminum with a sufficient S/N ratio. For this reason, aluminum products such as those shown in Fig. 6.9 can detect drill holes measuring φ0.3 mm in the interior of areas with an outer diameter of 100 mm. This is due to the utilization of an X-ray tube with a high target power tolerance for the focal point dimensions.

Among the devices listed in Table 6.1, there are some low-cost devices in the range of tens of thousands of USD made possible by technology transfers from the diffusion of dentistry X-ray CT scanners and the appropriation of their components. Figure 6.1g is one such example. Its characteristics include a lightweight main body at 50 kg, a size that can be placed on a desktop, and its compatibility with household power sources while being moved around on a cart. As shown in Fig. 6.10, application examples include various advances in disciplines where prohibitively expensive industrial X-ray CT scanners could not be frequently used, such as fundamental research on food product development, sports applications, and the confirmation of sport glove fit.

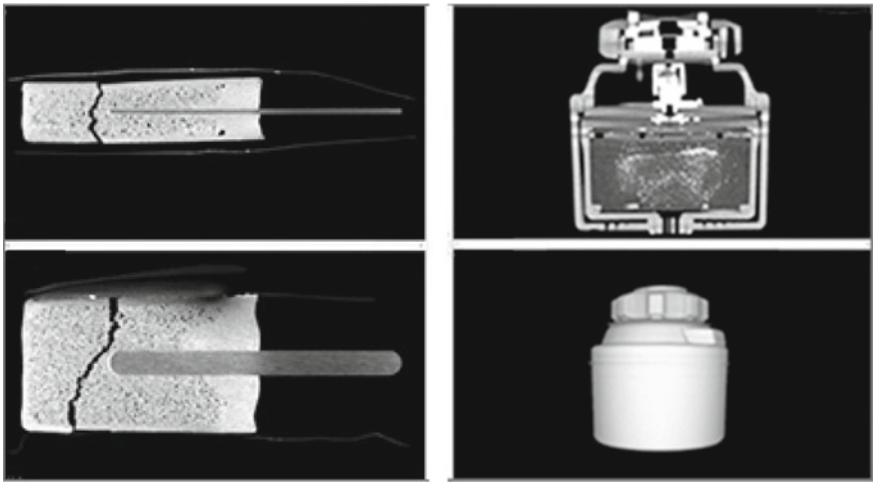

(a) (b)

Fig. 6.10 **a** Distribution of bubbles within a bar of ice cream. **b** is the observation of the internal structure of a water purifier. Miniature light-weight devices (RF Co. NAOMi-CT model) were used for both observations (courtesy of Kazumi Kodaira of RF Co.)

6.2 High-Energy Industrial X-ray CT Scanners

X-ray CT with X-ray energies in the MeV range has been developed and manufactured since the 1980s. Compact electron accelerators have been used as their radiation source. Devices that use radiation sources with energies of 950 kV, 3 MV, 6 MV, and 9 MV can be utilized as industrial products. Figure 6.11 shows an example of a commercially available product. These product specifications are recorded in Table 6.1. Devices with 12-MV radiation sources had been produced in the past but

Fig. 6.11 Example of a high-energy industrial-use X-ray CT scanner that is commercially available and described in Table 6.1. Photographs of the **a** Hitachi Co. HiXCT-9M model device and the HiXCT-1M, **b** shielding container, and **c** control panel/operating device (courtesy of Katsutoshi Sato of Hitachi Co.)

currently no longer exist. X-rays with MeV-level energies have a high penetrating power of materials, so decreased sensitivity in standard X-ray detectors is unavoidable. For this reason, line sensor detectors or detection circuits that are specialized for X-rays of MeV-level energies have been developed and implemented. This enables the acquisition of images with minimal artifacts due to low noise and a high dynamic range. The shape of the X-ray beam is a fan beam. For example, X-ray CT scanners with a drive voltage of 9 MV can observe steel and aluminum alloy materials with thicknesses up to 32 cm and 96 cm, respectively. The field of view is φ600–800 mm, the height 500–1000 mm, and a sample rotation stage with a load capacity of 100 kg is used. Proper shielding is necessary to prevent the leakage of high-energy X-rays in high-energy X-ray CT scanners out of the device. For example, the total weight of a 950 kV device can be up to 60–80 t when set up in a shielding container made of steel plates. Furthermore, the 9 MV machine can no longer be shielded with steel plates and must be housed in a reinforced-concrete shielding structure with 2 m thick concrete.

In addition to the so-called third-generation CT with a rotate/rotate system, measurement systems include the second-generation translate/rotate system and a new system referred to as the double-rotate system [2]. Fast imaging is characteristic of the rotate/rotate system, with speeds up to 10 s/slice. Meanwhile, the translate/rotate system is suited for imaging with a wide field of view but has a lengthy imaging time. Furthermore, the double-rotate system combines fast imaging and high-spatial-resolution imaging, requiring an imaging time that is approximately four times longer than the rotate/rotate system but with a spatial resolution that is superior by a factor of 1.5.

Figure 6.12 shows differences in image quality between scan systems. Innovations in the measurement system enable the clean visualization of difficult-to-detect

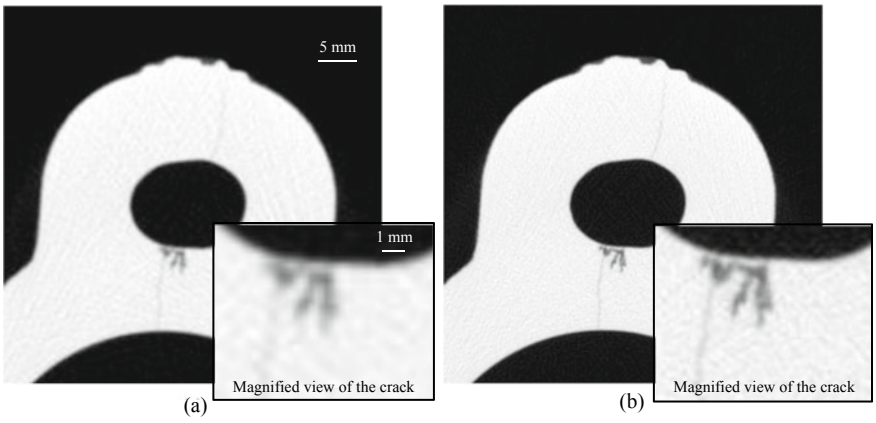

Fig. 6.12 Observation example of a cavity and crack in a cast iron component using a high-energy industrial-use X-ray CT scanner. Image **a** was obtained using the rotate/rotate system (pixel size 0.4 mm, 1500 × 1500 pixels, scan time 15 s) and **b** was obtained with the double-rotate system (pixel size 0.2 mm, 3000 × 3000 pixels, scan time 50 s). These were imaged using the Hitachi Co. HiXCT-9M-SP model (courtesy of Katsutoshi Sato of Hitachi Co.)

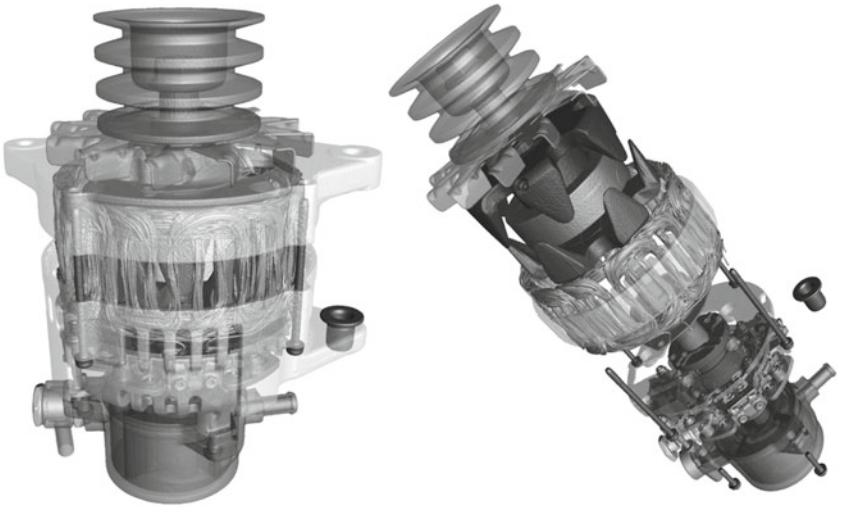

(a) (b)

Fig. 6.13 Observation example of an automobile component (alternator) interior using a high-energy industrialuse X-ray CT scanner; **a** is a 3D observation of the inner coil by making the external aluminum components semi-transparent and **b** is the segmentation of the constituent components, where each component is shown in a disassembled manner to show the assembly conditions. These were imaged using the Hitachi Co. HiXCT-9M-SP model (courtesy of Katsutoshi Sato of Hitachi Co.)

cracks with small openings in brittle cast iron parts. Furthermore, Fig. 6.13 shows a 3D imaging example of an automobile part. The noise and artifacts are sufficiently reduced while using high-energy X-rays, enabling not only the visualization of large-scale automobile part interiors but also assessments based on the segmentation and extraction/discrimination of its constituent components.

Fraunhofer EZRT operates an XXL-CT X-ray CT scanner, which can scan larger-scale products as is. This is shown in Fig. 6.14. XXL-CT is a device capable of conducting 3D imaging of automobiles, cargo containers, airplane fuselages, and large-scale ship engines as is. A rotation stage, which has a width of 3.2 m, height of 5 m, and load capacity of 10 t, is combined with 9 MeV high-energy X-rays to conduct 3D imaging with a focal spot size of approximately 3 mm. Automobiles are positioned upright on the rotation stage when conducting 3D imaging. It is anticipated that the applications of these types of CT scanners for large-scale structures will increase in the future.

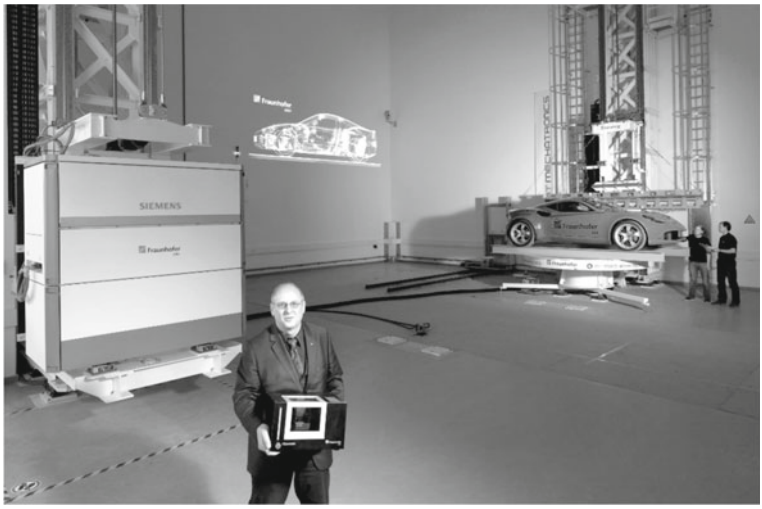

Fig. 6.14 X-ray CT scanner comprising an XXL-CT that can scan large automobile-scale products as-is, located in Fraunhofer EZRT in Germany (courtesy of Thomas Kessler of the Fraunhofer Laboratory)

6.3 High-Resolution Industrial X-Ray CT Scanners

Industrial X-ray CT scanners that seek high spatial resolutions using standard micro-focus tubes are introduced in Sect. 6.1. Industrial X-ray CT scanners that use X-ray focusing elements used in imaging-type X-ray micro-/nanotomography discussed in Sect. 5.1 are commercially available.

Figure 6.15 shows a visualization example of active materials in an electrode sheet of a commercially available secondary lithium-ion battery using an industrial X-ray CT scanner equipped with an imaging optical system that uses a Fresnel zone plate (introduced in Sect. 5.1.1) and an illumination system that uses a condenser zone plate. The internal 3D structure and voids between the particles can be clearly observed in Fig. 6.15. Observations and quantitative assessments of the opened and closed micropores are conducted from these images, as well as observations of internal structures closely associated with the performance and deterioration of the secondary lithium-ion battery including the debonding of the grain boundary between the primary particles accompanying the storage and discharge of lithium ions during lithium-ion battery charging and discharging. The device in Fig. 6.16, also recorded in Table 6.1, was used for this observation. This device uses a Fresnel zone plate with an outermost zone width of 35 nm and a nominal maximum spatial resolution of 50 nm. Observations in Fig. 6.15 show that the sample has a diameter of approximately 64 μm and a spatial resolution of 150 nm during imaging. The manufacturer has referred to this as a nano-resolution X-ray microscope and interpolates 3D imaging in the intermediate region between the micron-level spatial resolution

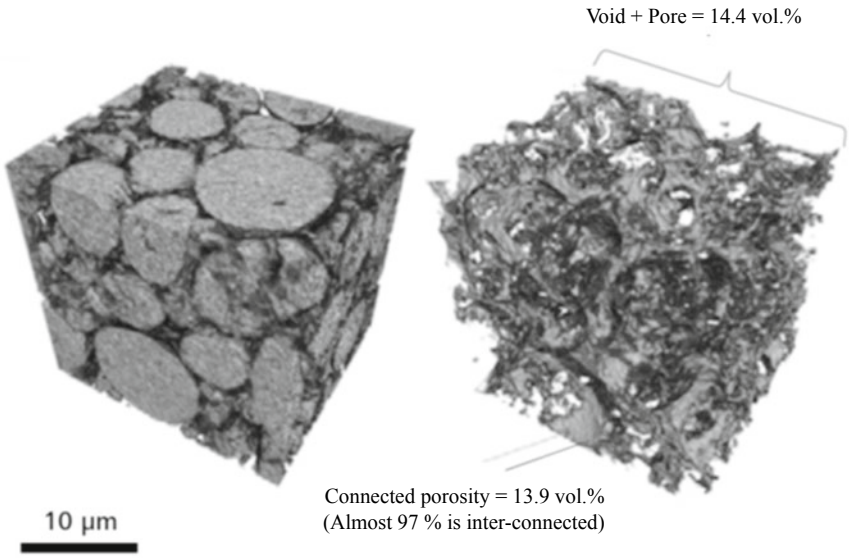

Fig. 6.15 Example where an electrode sheet was extracted from a commercially-available secondary lithium ion battery and where high-resolution visualizations of the 3D structure of active materials in an electrode (left) and inter-particle voids (right) were conducted. Imaging was conducted with a Carl Zeiss ZEISS Xradia 810 Ultra model (Fig. 6.16) (courtesy of Nobuhiro Hayami, Benjamin Hornberger, Stephen T. Kelly, and Hrishikesh Bale of Carl Zeiss Co.)

of microfocus X-ray CT and the nano-order region of electron microscopes. This device produces 3.5 keV monochromatic X-rays by using an approximately 0.9 kW high-brilliance X-ray source. According to the device manufacturer, chrome is used for the X-ray tube target and monochromatic characteristics with an energy resolution of approximately $\Delta E/E = 1.7 \times 10^{-3}$ are obtained through the combination of $K_{\alpha 1}/K_{\alpha 2}$ X-rays and a Fresnel zone plate. This enables an image optical system, which uses a Fresnel zone plate, to be achieved in commercially available industrial X-ray CT scanners. A phase plate is inserted in the optical path to set up a Zernike phase contrast microscope (discussed in Sect. 5.2.2). A stage with an in situ observation device introduced in Sect. 4.5 can be used for the sample rotation stage and in situ observations of tension, compression, and nano-indentations can be made. There are considerable limits with regards to sample size, however, this has been applied in a wide range of disciplines, including material development (e.g. polymers, ceramics, and batteries), natural resource exploration (e.g. oil and minerals), and bioengineering.

Fig. 6.16 Example of a commercially-available high-resolution industrial-use X-ray CT scanner described in Table 6.1. This is the Carl Zeiss ZEISS Xradia 810 Ultra model (courtesy of Nobuhiro Hayami of Carl Zeiss Co.)

6.4 High-Functionality Industrial X-Ray CT Scanners

The previous section detailed how considerably high spatial resolutions could be obtained in absorption contrast tomography using industrial X-ray CT scanners equipped with a microfocus X-ray tube. However, there are occasionally instances with various observation subjects where the contrast is low and observations cannot be made or where there are problems with regards to quantitative assessment. Of the polycrystalline structure tomography methods introduced in Sect. 5.5, the diffraction contrast tomography in Sect. 5.5.2 can be implemented at the laboratory level by using products that incorporate modules and analysis software specific to industrial X-ray CT scanners.

Figure 6.17 shows a 3D visualization example of a crystallographic structure of polycrystalline iron. A clean 3D visualization is obtained without gaps or overlaps in the crystallographic grains, which have a crystallographic grain diameter of approximately 100 μm. This enables not only the accurate determination of the 3D

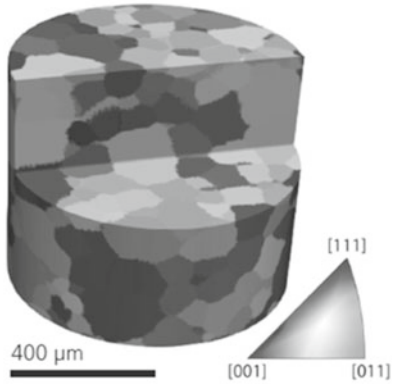

(a) 3D polycrystalline structure and corresponding inverse pole figure

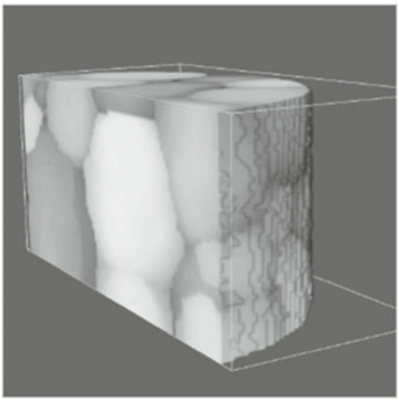

(b) Halved 3D image

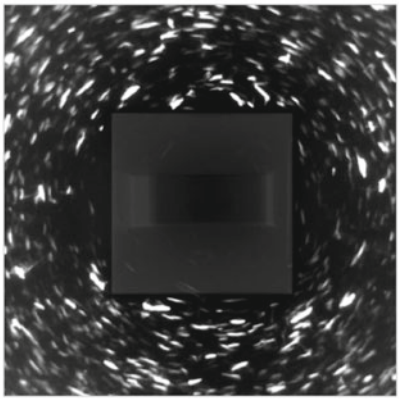

(c) Diffraction pattern of grains

Fig. 6.17 **a** and **b** are 3D images of the polycrystal structure of polycrystalline iron. The colors of each crystallographic grain indicate the crystal orientations expressed in the inverse pole figure included in **a**. The Carl Zeiss ZEISS Xradia 520 Versa model (Table 6.1 and Fig. 6.18 for reference) was used for imaging (courtesy of Nobuhiro Hayami of Carl Zeiss Co.)

morphology of the crystallographic structure but also crystallographic assessments of various physical phenomena (e.g. recrystallization/growth behavior, relationships between crystallographic structure and various mechanical properties/corrosion characteristics).

Figure 6.18 shows a photograph of the industrial X-ray CT scanner used for imaging in Fig. 6.17. The basic structure of the device is the same as that of an industrial X-ray CT scanner with a standard microfocus X-ray tube. This device adopts a scintillator and a detector that uses an objective lens from an optical microscope in a manner similar to synchrotron radiation X-ray tomography. In other words, the device combines geometric X-ray magnification projection using a microfocus X-ray

Fig. 6.18 Example of a commercially available high-functionality industrial-use X-ray CT scanner described in Table 6.1. This is the Carl Zeiss ZEISS Xradia 520 Versa model (courtesy of Nobuhiro Hayami of Carl Zeiss Co.)

tube with an optical image converted to visible light. A geometric magnification in the order of 100:1 is usually necessary to achieve a spatial resolution below 10 μm with micro-tomography using a microfocus X-ray tube. Meanwhile, this device can control the geometric magnification based on the cone beam optical system to a factor of 1–10 and achieves a larger working distance by magnifying after visible light conversion. This enables the implementation of material tests that use relatively large testing devices and in situ observations under heating or electrification even among the in situ observation devices introduced in Sect. 4.5. An aperture plate and beam stop can be installed during diffraction contrast tomography to detect only diffracted light while shielding 0th-order light. An X-ray diffraction pattern as is shown in Fig. 6.17c is then obtained while rotating the sample. This allows for the acquisition of geometric information such as crystal coordinates, orientation, size, and morphology of crystallographic grains with a minimum grain size of around 40 μm and an angular resolution of the crystallographic orientation of 0.5°. Standard absorption contrast tomography imaging can also be conducted in the same sample; therefore, the relationships between the crystallographic structure obtained from diffraction contrast tomography and the cracking obtained from absorption contrast tomography can be directly assessed as well.

6.5 In-Line Inspection Device

The objectives of in-line inspections are to measure the dimensions/shape of products, components, and substrates that move down a mass-production production line, identify the presence of defects, and conduct quality control. If these can be conducted for the inspection of all products, the delivery of defective products can be prevented, significantly impacting product reliability. In addition to human-based inspections, in-line inspections until now have involved external appearance inspections with visible-light cameras, transmission image inspections using X-rays, and robot-based measurements. Line sensor cameras introduced in Sect. 4.4.2 (1) are widely used for in-line inspections based on transmission images.

Since the start of the twenty-first century, X-ray CT scanners and similar technologies have been used for in-line inspections during the production process of automobile parts, semiconductors, and electric circuits. The wafer implementation process, which falls under the post-processing step of the semiconductor production process, is the primary subject for these types of technology. Furthermore, the multiple soldered parts in electric circuits (e.g. solder wetting defects, through-hole packing defects, or insufficient soldering amounts) are frequently the source of production defects. Figure 6.19 is an example of such a fast X-ray CT-type automatic inspection device. Its specifications are described in Table 6.1. Its output is small as its primary subjects are substrates; an air-cooled sealed-type microfocus X-ray tube is used here. Due to

Fig. 6.19 Photograph of an in-line inspectionuse X-ray CT scanner described in Table 6.1; Omron VT-X750 model (courtesy of Nobuharu Sugita of Omron)

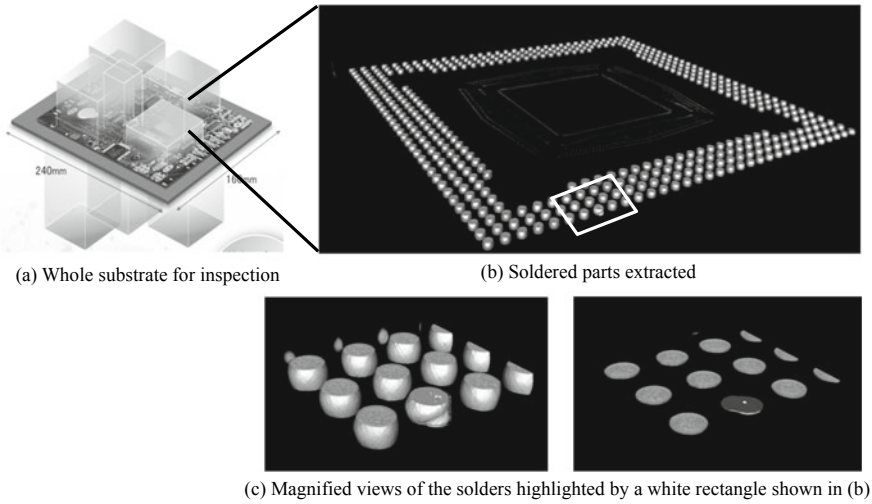

(a) Whole substrate for inspection

(b) Soldered parts extracted

(c) Magnified views of the solders highlighted by a white rectangle shown in (b)

Fig. 6.20 Inspection example of a soldered section of the electric circuit using a commercially available in-line inspection X-ray CT scanner (Omron VT-X750 model) shown in Table 6.1 (courtesy of Nobuharu Sugita of Omron)

its high spatial resolution, this single unit is capable of conducting not only mass-production inspections but also analyses of defective products diverted as a result of mass-production inspections. This device is unique in that it applies a specialized measurement system referred to as parallel CT [1]. This involves the turning of the camera and sample in a circular trajectory that is parallel to the substrate instead of a rotation stage. This enables fast tomography wherein a single 3D image can be obtained in 4 s. Although the device in Fig. 6.19 is for in-line inspection, there is also a high-spatial-resolution (0.3 μm/pixel) device for off-line inspection. Figure 6.20 shows the verification of soldering junction strength using the device in Fig. 6.19. A single defective part was identified from several hundred soldered sections, in which pore-like defects were visible in its interior.

Figure 6.21 also shows an inspection device that is specialized for the in-line inspection of electric circuits, with a structure that combines X-ray tomography, X-ray transmission inspections, visible-light/infrared microscopy observations, and laser distance measurements [3]. The in-line setup of this device in an electric circuit production line enables X-ray tomography observations at a spatial resolution that is high enough for detailed soldering junction inspections while simultaneously identifying marks due to visible/infrared light and X-ray observation reference plane measurements using a laser range finder. This device has the characteristic of being able to conduct fast imaging that can keep up with the production line cycle time despite taking such a high number of measurements simultaneously. Figure 6.22 is a summary of the information obtained from each of these inspections. This device is capable not only of detecting various production defects such as the presence of voids in a heat sink or back fillet of leads, but also various defective product ejections

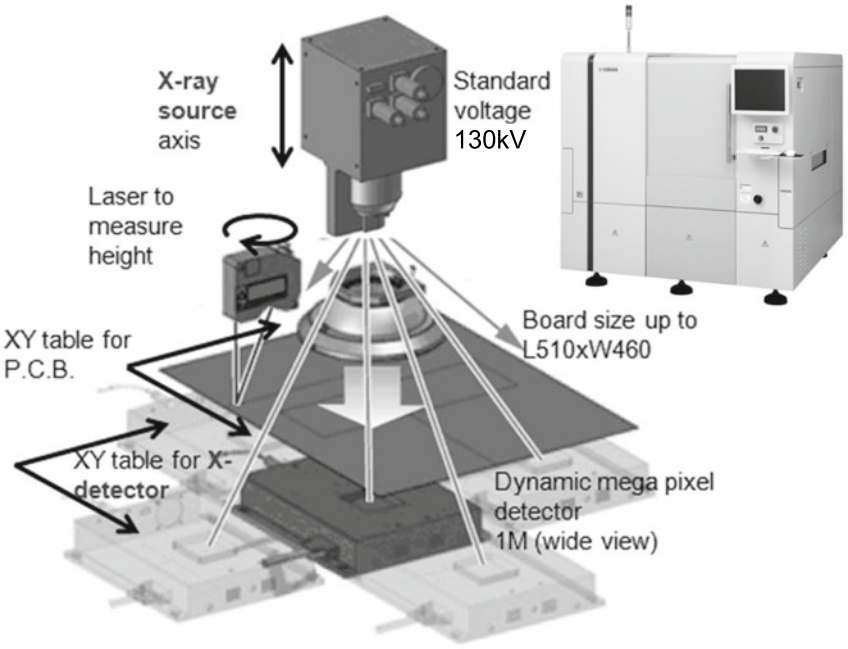

Fig. 6.21 Photograph (top right) of a commercially available in-line inspection-type X-ray CT scanner described in Table 6.1 and an internal layout where visible-light inspection, laser displacement sensor, and an X-ray imaging system co-exist; Yamaha Motor Company Tsi-X model (courtesy of Akira Kakuta of Yamaha Motor Company)

and traceability assurances such as serial number identification and the detection of product assembly errors, all simultaneously and autonomously. Furthermore, despite using a sealed tube, the device is innovative regarding its maintenance as the X-ray tube filament is exchanged and rebuilt when the filament is broken.

Meanwhile, Fig. 6.23 shows an X-ray CT scanner that is built for imaging with standard X-ray tomography. Its specifications are listed in Table 6.1. This device uses a high-output X-ray tube and is used for the complete part-by-part inspection of products like aluminum alloy components. Despite conducting standard X-ray tomography, it is capable of conducting fast imaging at speeds of 1 min/scan, which correspond to the production lines of automobile components. Figure 6.24 shows an observation example where this device was used to observe internal defects (e.g. cavities) in the interior of an aluminum die-casting product. This device can be set up even in harsh usage environments that would be harsh for precision instruments due to temperature or dust, like in aluminum die-casting lines. Inspections are conducted from when the casting product enters the inside of the device until the product quality is determined, as this is synchronized with the production cycle of die-cast machines. In addition to manual inspections by staff members, there are also

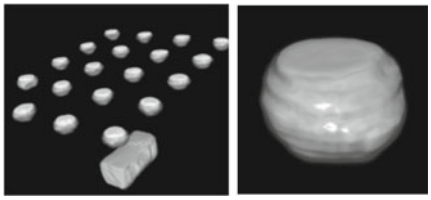

(a) High-speed sliced surface inspection using X-ray tomography

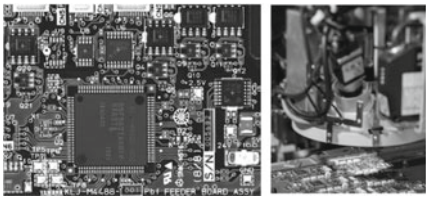

(b) High-speed optical microscope image obtained simultaneously with X-ray tomography images

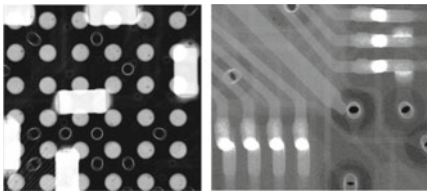

(c) X-ray radiographs obtained simultaneously with the optical inspection

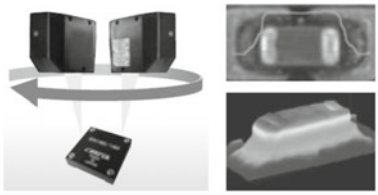

(d) Laser height position measurement

Fig. 6.22 Inspection example of an electric circuit using a commercially available in-line inspection-type X-ray CT scanner (Yamaha Motor Company Ysi-X model) described in Table 6.1. X-ray tomography, X-ray transmission, optical microscopy observations, infrared light observations, and laser inspections can be conducted simultaneously (courtesy of Akira Kakuta of Yamaha Motor Company)

Fig. 6.23 Photograph of a commercially available in-line inspection-type X-ray CT scanner described in Table 6.1; JED CTH200FPD model (courtesy of Osamu Kinoshita of JED, Co., Ltd.)

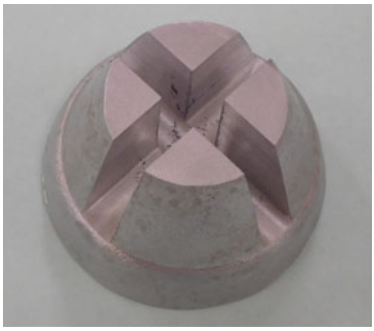

(a) Test piece for inspection

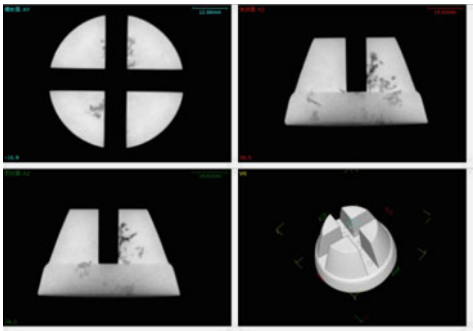

(b) Inspection of blow holes using a 3D image and virtual cross sections

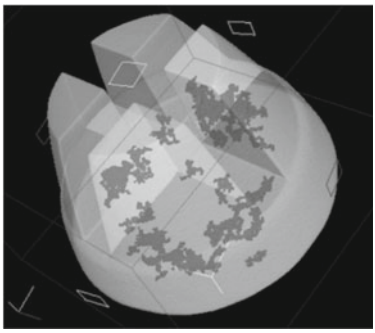

(c) 3D rendered blow holes

Fig. 6.24 Inspection example of an aluminum die-cast component using a commercially available in-line inspection-type X-ray CT scanner (JED CTH200FPD model) described in Table 6.1 (courtesy of Osamu Kinoshita of JED, Co., Ltd.)

completely automated inspections conducted in coordination with industrial robots. Product inspections can immediately and automatically determine the quality of all products while automatically saving and recording various numerical data, which can be used for subsequent defect dimension measurements.

6.6 X-Ray Tomography Using Synchrotron Radiation

The current state of the technology used at the imaging beamlines in SPring-8 and the Photon Factory, as well as recent application examples, is introduced here.

6.6.1 Projection-Type X-Ray Tomography

Projection-type X-ray tomography can be implemented at SPring-8 primarily through the two beamlines of BL20XU and BL20B2. The former is a beamline that uses an undulator and is suited for high-resolution work, whereas the latter is a beamline that uses bending magnets and is suited for imaging with a wide field of view. Both beamlines primarily use a 2048 × 2048-pixel Hamamatsu Photonics sCMOS camera measuring 6.5 μm × 6.5 μm. The former is often combined with a BM-3 beam monitor that combines a scintillator with a visible-light lens and mirror. The latter frequently uses a BM-2. Combinations of different beam monitors allow for changes in the effective pixel size. As can be observed later in Fig. 7.15, the effective spatial resolution for both cases is exactly double that of the pixel size (approximately 0.5 μm for projection-type X-ray tomography in BL20XU) [23]. In other words, the spatial resolution is limited by the Nyquist frequency, which is based on the sampling theorem (discussed in Sect. 7.5.1 (2)).

Figure 6.25 shows an imaging example using BL20B2 [4]. Beamlines that use bending magnets are more suited for metals even if they are porous with over 90% porosity. The effective pixel size, in this case, is 2.7 μm, the spatial resolution is 5.4 μm, and both the field of view width and height are 5.4 mm. Clean visualizations of not only the complex and irregular structure of the porous metal cell wall but also of the interior micropores and precipitated hydrogen was obtained. With the support of the 3D image-based simulations (discussed in Sect. 8.6), this research has elucidated the deformation/fracture behavior of porous metals.

BL20XU is used when further spatial resolution is required. Figure 6.26 shows a visualization of creep fracture behavior in steel materials at high temperatures. The effective pixel size, in this case, was 0.5 μm, the spatial resolution was approximately 1.0 μm, and both the field of view width and height were approximately 1 mm. Exposure to high temperature after heat-resistant steel with 9% chrome was welded created defects referred to as type IV voids in the heat-affected zone. This was observed at 650 °C under a load of 70 MPa after 17,220 h. Defects (creep voids) occurred at the specified grain boundary of the prior austenite and the formation of voids, which had not been recognized until now, were observed in the crystallographic grains. Micro-scale voids were extremely clearly captured and the various 3D/4D analysis methods in Chaps. 8 and 9 can be used.

Figure 6.27 shows the observations of the inner pyramidal layer in the cortex of the frontal lobe of the human brain using BL20XU [5]. Absorption contrast with an X-ray energy of 12 keV was used for observation. The effective pixel size, in this case, was 0.51 μm and the effective spatial resolution was 1.2 μm. The top area of Fig. 6.27 corresponds to the brain surface. These observations clearly show the pyramidal neuron, which is the primary excitatory neuron that exists in the cerebral cortex and hippocampus [5].

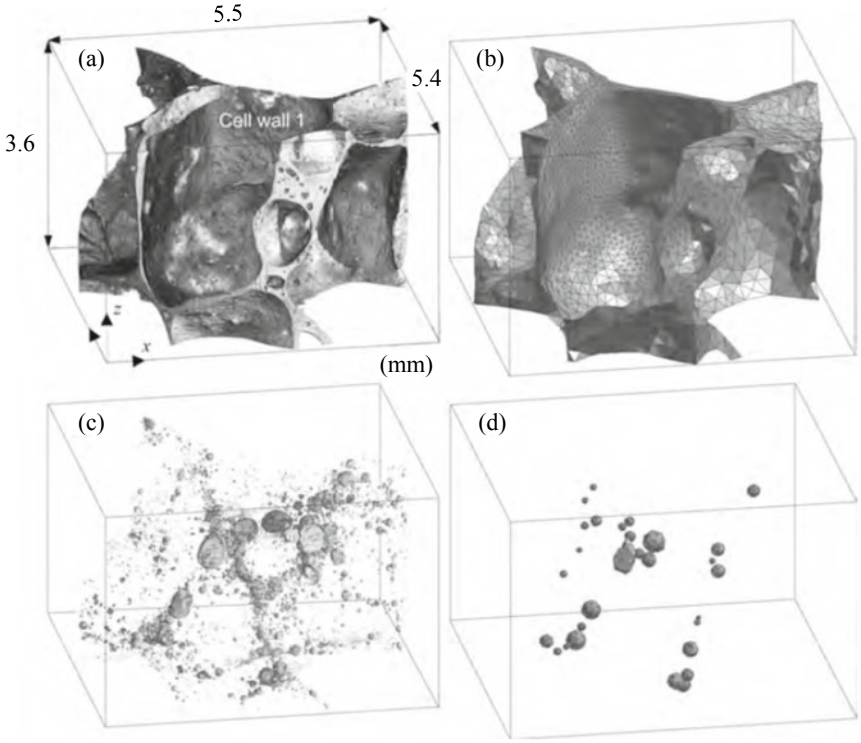

Fig. 6.25 Observation example using BL20B2 in SPring-8. The X-ray energy at BL20B2 was set at 20 keV and 3D imaging was conducted at experimental hutch 1 with an effective pixel size of 2.73 μm [4]. The observation subject was porous aluminum; **a** and **c** show the porous metal cell wall and the interior pores; **b** and **d** show the surface extractions for image-based simulations (STL files)

6.6.2 Imaging-Type X-Ray Tomography

Experimental devices for imaging-type X-ray tomography have been made available to users since the mid-2000s at a number of imaging beamlines in SPring-8. Throughout the 10 years following this period, imaging with relatively low X-ray energies of 8–10 keV has been conducted for various applications. Figure 6.28 shows the observation results of precipitates in aluminum conducted during this early stage [6]. Precipitates in Al–Ag alloys have been observed at high spatial resolution in this research. Imaging-type X-ray tomography experiments were exclusively conducted at BL47XU at the time, with the illumination system comprising a parallel beam passing through a diffusion plate; Köhler illumination had not yet been used. The effective pixel size, in this case, was 88 nm and an effective spatial resolution approximately double this was obtained. However, the sample size was 56.8 μm (H) ×

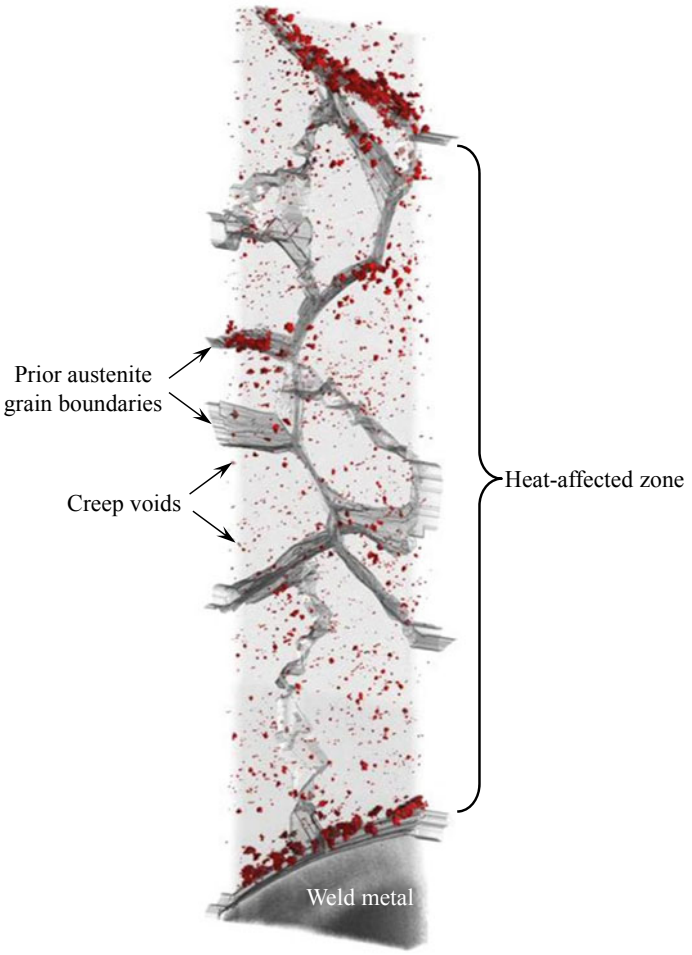

Fig. 6.26 Observation example using BL20XU at SPring-8. The X-ray energy was set at 37.7 keV and 3D imaging was conducted at experimental hutch 1 with an effective pixel size of 0.5 μm. The observation subjects are the type IV voids formed by creep of the welded material of the high-chrome heat-resistant steel

35.3 μm (V) and thinner than the width of a hair due to the X-ray energy limitations of 9.8 keV, as there was considerable difficulty in sample preparation and handling.

Subsequent research and development on imaging-type X-ray tomography at SPring-8 has continued in earnest, with 3D imaging that uses 20-keV and 30-keV X-ray energies achieved in 2017 and 2018, respectively. Currently, imaging-type X-ray tomography can be conducted at BL47XU and BL37XU, with BL20XU at the center. The mainstream setup is as shown in Fig. 5.25, which is phase-contrast imaging-type X-ray tomography that combines Köhler illumination, a Fresnel zone

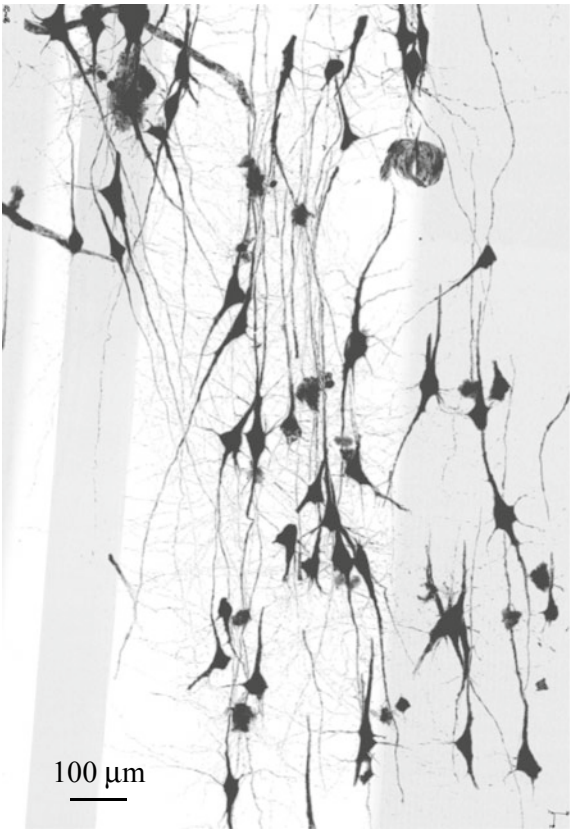

Fig. 6.27 Observation of the inner pyramidal layer of the cortex of the frontal lobe in the human brain using BL20XU at SPring-8 [5]. The X-ray energy was set at 12 keV (courtesy of Ryuta Mizutani of Tokai University)

plate, and a Zernike phase plate. SPring-8 is equipped with a condenser plate, Fresnel zone plate, and phase plate, all of which are suited to high-energy usage but are difficult to micromachine. The realization of the apodization Fresnel zone plate (discussed in Sect. 5.1.1 (3)) in particular is key to achieving high-energy imaging-type X-ray tomography. BL20XU can now switch between projection and imaging modes at a touch. It may appear like there are no major differences between this facility and the imaging-type X-ray tomography of other facilities with regard to spatial resolution. However, as discussed in Sect. 7.5.3 (1), other reports on spatial resolution measurements have not frequently accurately identified and measured single cycles in the periodic structure of the test object from the image data and instead displayed half of this as the spatial resolution. Sufficient care must be taken when comparing performance based on reports from different institutions.

Figure 6.29 shows an observation example of nanovoids that formed during hydrogen embrittlement in an aluminum alloy. Combinations of imaging-type X-ray tomography, projection-type X-ray tomography, and HAADF-STEM have enabled observations of the formation of high-density nanovoids across multiple scales, from several nm to 10 μm [7]. In addition to these types of direct observations, nanovoid

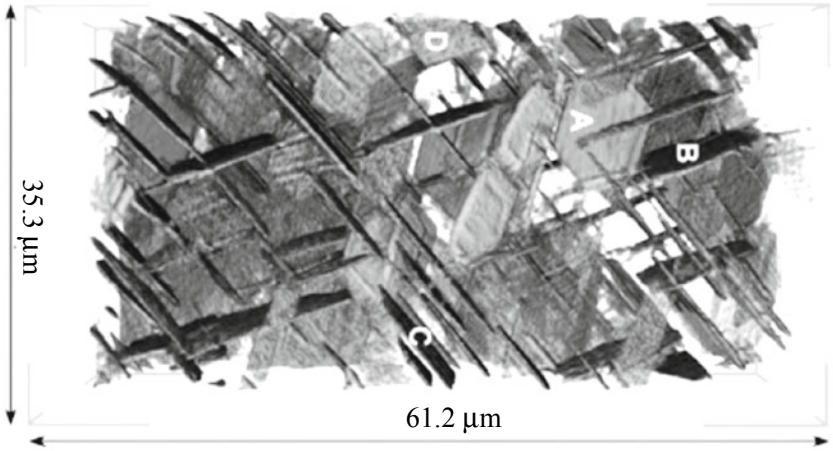

Fig. 6.28 Observation example using BL47XU at SPring-8 [6]. The X-ray energy was set at 9.8 keV and 3D imaging was conducted with an effective pixel size of 88 nm. Observation subjects are aging precipitates in over-aged Al-Ag alloy material

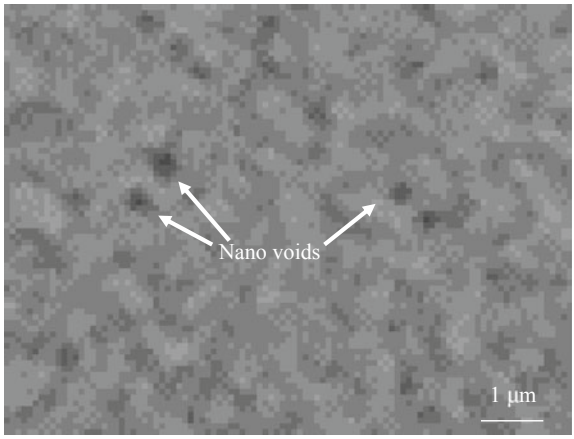

Fig. 6.29 Observation of nanovoids formed during hydrogen embrittlement of A7150 aluminum alloys using BL20XU at SPring-8. The X-ray energy was set at 20 keV and 3D imaging was conducted with an effective pixel size of approximately 60 nm

formation and growth can be perceived as the generation of tensile strains under hydrostatic pressure, as shown later in Fig. 9.13 [7].

Figure 6.30 shows imaging-type X-ray tomography-based observations of the cortex of the frontal lobe in a human brain, observed in Fig. 6.27 with projection-type X-ray tomography (separate sample). The experiment, in this case, was conducted using BL37XU, the X-ray energy was 8 keV, and the effective spatial resolution was 100 nm. Absorption contrast was used in the imaging method. The pyramidal neurons in the cortex of the frontal lobe in the human brain and the surrounding neurites can be clearly observed. Furthermore, the spinous process can be observed in the neurite.

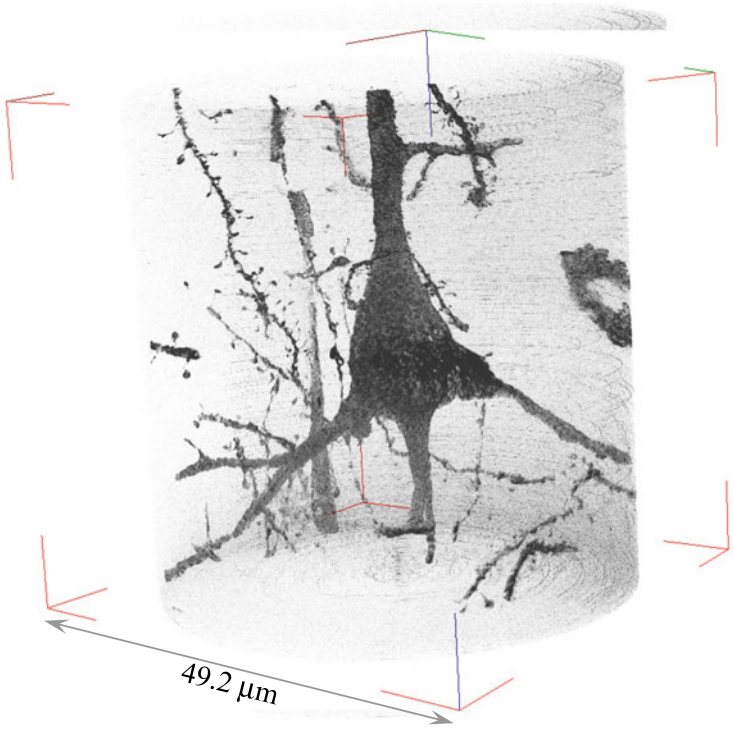

Fig. 6.30 Imaging X-ray tomography observations at BL37XU at SPring-8 of the inner pyramidal layer in the cortex of the front lobe in the human brain, which was observed with projection X-ray tomography in Fig. 6.27 [5]. The X-ray energy was set at 8 keV (courtesy of Ryuta Mizutani of Tokai University)

The spinous process is formed or destroyed depending on neural activity in the brain and the observations of its number and morphology are important for understanding the mechanisms of neural pathway formation.

6.6.3 Phase-Contrast Tomography

Imaging beamlines at SPring-8 currently requires either a combination of projection-type X-ray tomography and the single-distance phase retrieval method (discussed in Sect. 5.2.1 (2)) or imaging-type X-ray tomography that uses a Zernike phase-contrast microscope (discussed in Sect. 6.6.2). First, Fig. 6.31 shows an observation example of the former with DP steel using methods employed by Paganin [8]. This is a DP steel that comprises a dual-phase structure of martensite and ferrite, where observations of deformation, damage, and fracture behavior under tensile loads are observed in a material where the martensite has a volume fraction, which barely forms a 3D

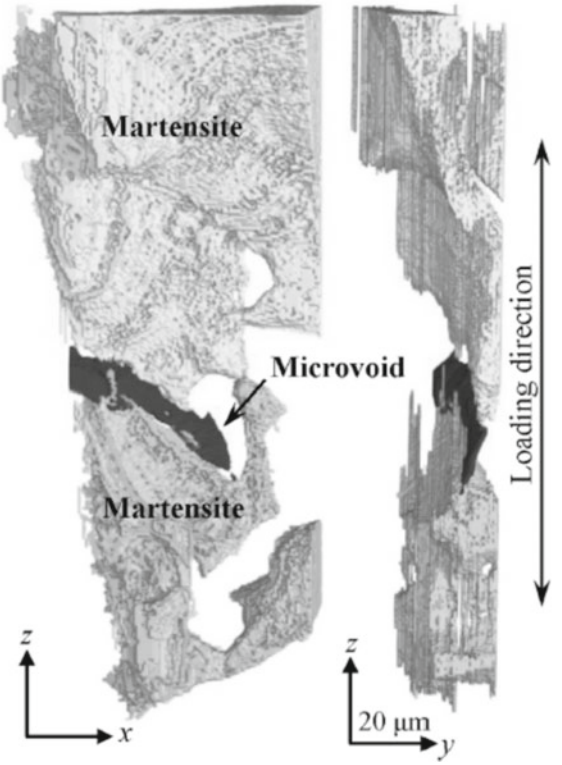

Fig. 6.31 In-situ observation example of martensite phase damaging behavior in DP steel using BL20XU at SPring-8 [8]. The X-ray energy was set at 37.7 keV and 3D imaging was conducted with an effective pixel size of 0.5 μm. The gray areas in the figure are the martensite phases and the black areas are crack-like voids where the martensite phase was fractured. The original figure is in color; please refer to the original publication for details

network. The carbon concentration in the martensite phase is approximately 0.33%, whereas the carbon concentration in ferrite is low at approximately 0.001%. As such, the martensite and ferrite phases have densities of 7.87 and 7.76 g/cm^3, with a difference of approximately 1.4% between them. The imaging in Fig. 6.31 uses this density difference. Discrimination between the two phases in ferrite-pearlite steel, which has a density difference of approximately 0.4%, is possible with this method [9].

Figure 6.32 shows a visualization of a retained austenite phase in TRIP steel using a Zernike phase-contrast microscope. In Fig. 6.32a, where phase retrieval of the projection-type X-ray tomography was conducted using Paganin's methods, the presence of the austenite phase could be visualized; however, its morphology was unclear. Meanwhile, imaging-type X-ray tomography using a Zernike phase-contrast microscope enabled the visualization of the morphology of the austenite phase with sufficient spatial resolution and contrast. This research captured the gradual changes in the austenite phase. It is anticipated that findings valuable for microstructural design will be obtained in the future.

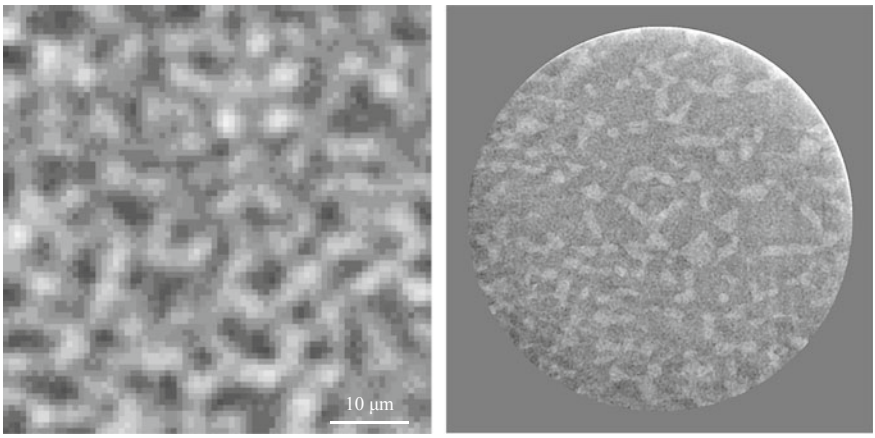

(a) Projection-type X-ray tomography image that has been phase-retrieved by means of Paganin's method

(b) Sample in (a) observed using imaging-type X-ray microtomography technique combined with Zernike phase-contrast optics

Fig. 6.32 Observation example of the austenite phase in TRIP steel using BL20XU at SPring-8 [8]. The X-ray energy is set at 20 keV and in-situ observations of the deformation-induced austenite transformation while the specimen is under tension are shown. The effective pixel size in **b** is 60 nm. Phase retrieval with Paganin's method after projection X-ray tomography imaging with an effective pixel size of 0.5 μm is shown for comparison in **a**. Both are shown with the same magnification

6.6.4 Fast Tomography

Examples conducted by the author at ESRF using white X-rays will be introduced here for fast tomography. Figure 6.33 shows in situ observations of fracture toughness tests conducted on an A2024 aluminum alloy [10]. Changes in the distribution of the driving force for crack propagation can be observed. Fixing the displacement each time X-ray tomography imaging is conducted results in unloading during in situ observations of metal material fracture due to relaxation phenomena. Elasto-plastic analysis applications for the obtained 3D images cannot be validated for experiments, which experience unloading. This research took single scans every 22.5 s, which was, at the time, an extremely accelerated setup, through the combination of white light, a camera capable of high-speed readout, and an imaging process that minimized time loss. The research conducted in situ observations of crack propagation during fracture toughness experiments conducted at a fixed cross-head speed without any interruptions and analyzed the strain field of the crack tip. These methods were used to reduce imaging time for a single 3D image by 1/50th of the original duration while maintaining superior spatial resolution when a monochromatic X-ray was used. The obtained images visualized not only cracks but also microstructures such as particles. As shown in Fig. 6.33, this enabled the clear visualization of crack tip morphology corresponding to stress-field singularities of the crack tip (i.e. crack-tip blunting/sharpening), as well as the transitions and spatial spread of stress-field singularities accompanying crack propagation.

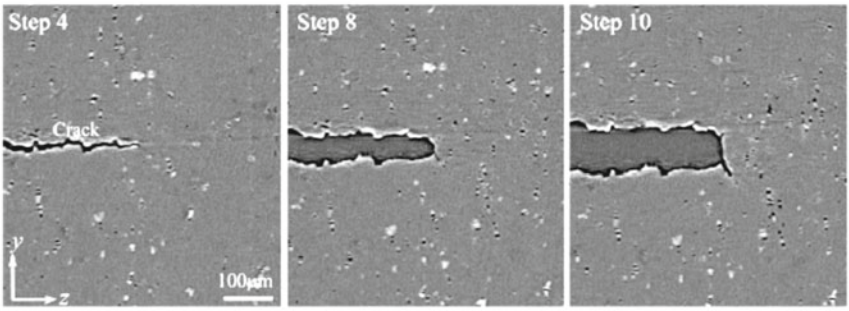

(a) Cross-sections at $x = 59$ μm (An example of remarkable crack-tip blunting)

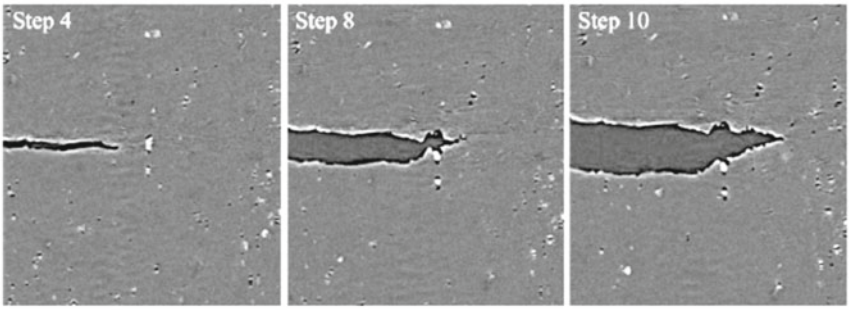

(b) Cross-sections at $x = 577$ μm (An example of sharp crack-tip during propagation)

Fig. 6.33 In-situ observations of fracture toughness experiments of a fatigue pre-cracked A2024 aluminum alloy using the ID15A beamline at ESRF [10]. Blunting (top row) and sharpening (bottom row) of the propagating crack tip can be observed by continuously conducting fast tomography observations while applying tensile loads without any unloading

6.6.5 Tomography of Elemental Concentrations

Figure 6.34 shows the application of absorption-edge subtraction imaging introduced in Sect. 5.4.1 on an Al–Si–Cu ternary alloy after a high-temperature solution-treatment, as well as the quantification of the spatial distribution of copper concentrations in the microstructure and its relationship with fracture [11]. A 3D image was obtained at the X-ray energies above and below the K-absorption edge of copper (upper side: 9.038 keV, lower side: 8.938 keV), on which pixel subtraction was conducted. The Al–Si–Cu ternary alloy exhibited the highest strength at 807 K as a solution-treated sample when the solution treatment temperature was varied between 773 and 824 K and both a tensile strength improvement of over 12% and reduction in solution treatment time of approximately 1/5th were achieved relative to the standardized heat treatment conditions (T6 treatment) [11]. This temperature corresponds to a range above the ternary eutectic point and significant increases in copper concentration, pore formation/growth, and matrix copper concentration were observed due to local melting such as in Fig. 6.34. This research shows that pores formed from eutectic melting deteriorate material characteristics and act as preferential pathways

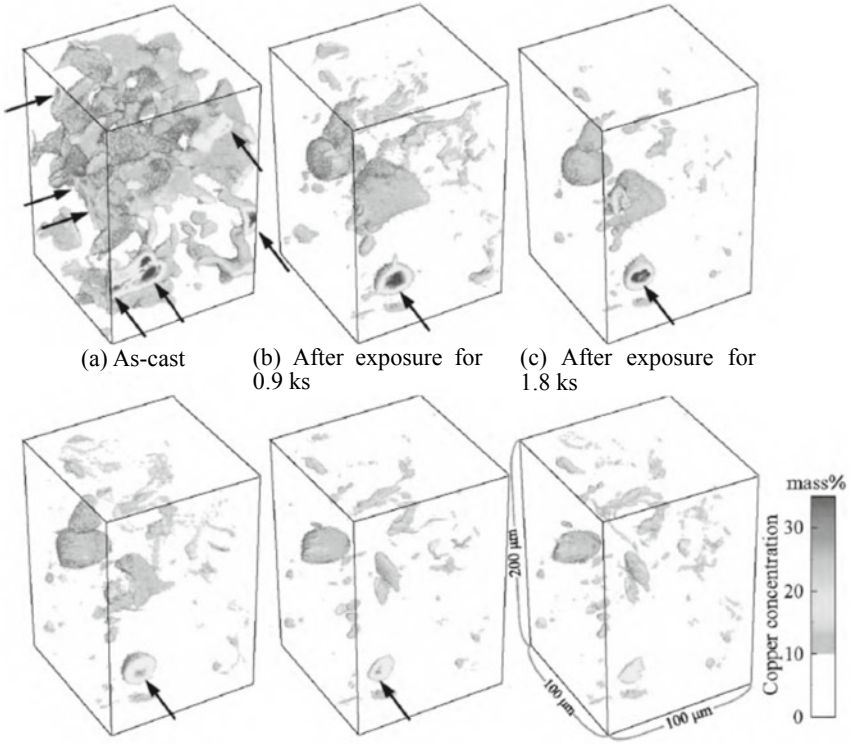

Fig. 6.34 Changes in the microstructure during solution treatment at a temperature of 807 K, where the pure ternary system Al–Si–Cu alloy has the highest strength when solution treatment temperatures varied between 773 and 824 K. Absorption-edge subtraction imaging was used for 3D mapping of copper concentration distributions [11]. The original figure is in color; please refer to the figure of the original publication for details

for crack propagation [11]. However, it was also demonstrated that the beneficial effects of increased precipitate due to increased copper concentration outweigh the negative effects of local melting when heat treatment is applied for a short period even if above the ternary eutectic point and that this results in the improvement of the material characteristics [11].

Other applications of absorption-edge subtraction imaging involve the visualization of alloy element distributions in the cell walls of cast porous metals [12] and the mapping of tungsten concentration distributions in steels [13].

An imaging-type XAFS tomography setup can be utilized at the PF-AR NW2A beamline in the Photon Factory; Fig. 6.35 shows this setup. A Carl Zeiss X-ray microscope Xradia Ultra was introduced in this beamline and X-ray energies of 5–11 keV can be used. Figure 6.36 shows observations of Yb–Si–O particles prepared

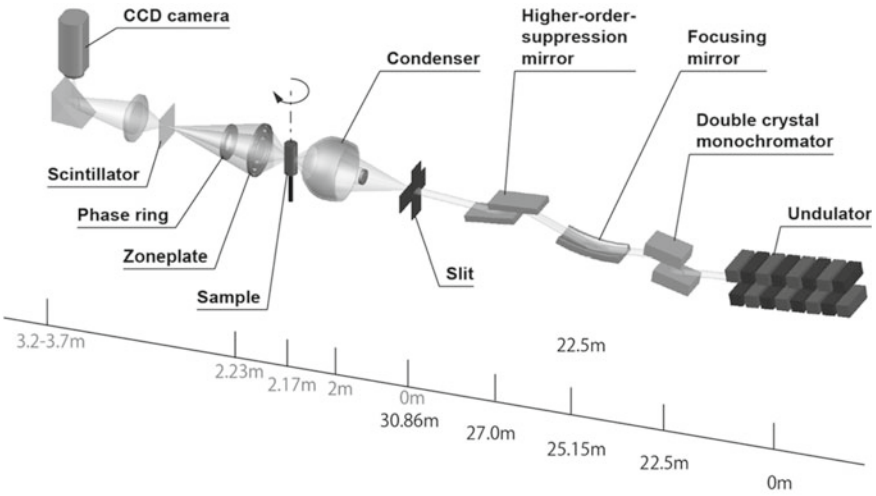

Fig. 6.35 Imaging XAFS tomography setup, which can be used at the Photon Factory (PF-AR NW2A beamline) (courtesy of Masao Kimura of KEK)

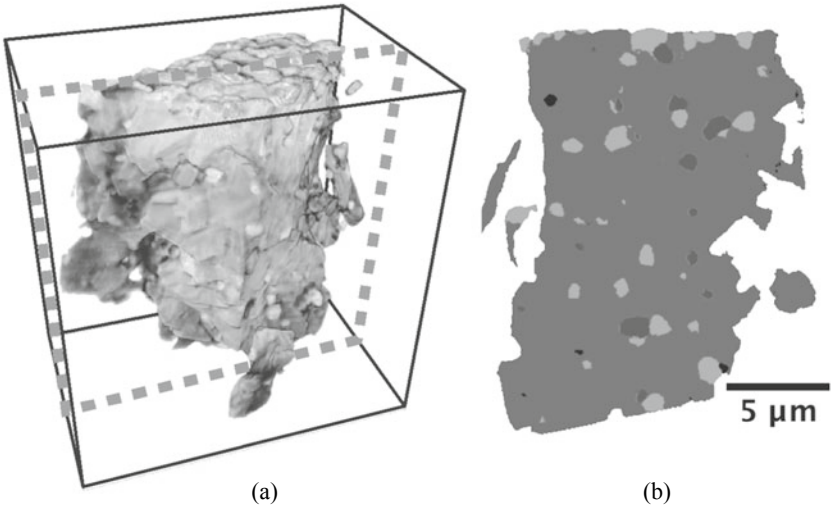

Fig. 6.36 X-ray microscopy observation results where an $Yb_2Si_2O_7$ oxidized plate was heated at high temperatures. **a** 3D image at an X-ray energy of 8.98 keV. **b** Results where the chemical conditions of Yb were differentiated using measurements that combine X-ray CT and X-ray absorption spectroscopy (XAFS-CT) (corresponds to the cross-section of the dotted lines in **a**). The reference has a color figure; please refer to this figure for details (courtesy of Masao Kimura of KEK) [14]

by pulverizing that measure 10–20 μm in diameter [14]. X-ray tomography imaging was conducted at 36 X-ray energy levels near the L_{III} absorption of Yb (8.9–9.06 keV) and a 3D image with a pixel size of 48.8 nm was obtained. This research succeeded in cleanly distinguishing the chemical states of Yb in the sample interior [14].

6.6.6 *Tomography for Polycrystalline Structures*

Figure 6.37 shows an example of the X-ray diffraction-amalgamated grain-boundary tracking (DAGT) introduced in Sect. 5.5.4 being applied to the crystallographic analysis of fatigue crack propagation in aluminum alloys for airplanes [15]. Fatigue crack propagation is heavily influenced by crystal structure even in stage IIb of fatigue crack propagation, which is generally considered insensitive to microstructure; cracks were shown to have deflections or to be twisted in the grain boundaries where large differences in crystallographic orientation were observed. Furthermore, acceleration and deceleration due to the crack closure patches at the crystallographic grain boundary or crack tip vicinity were microscopically observed. A particularly

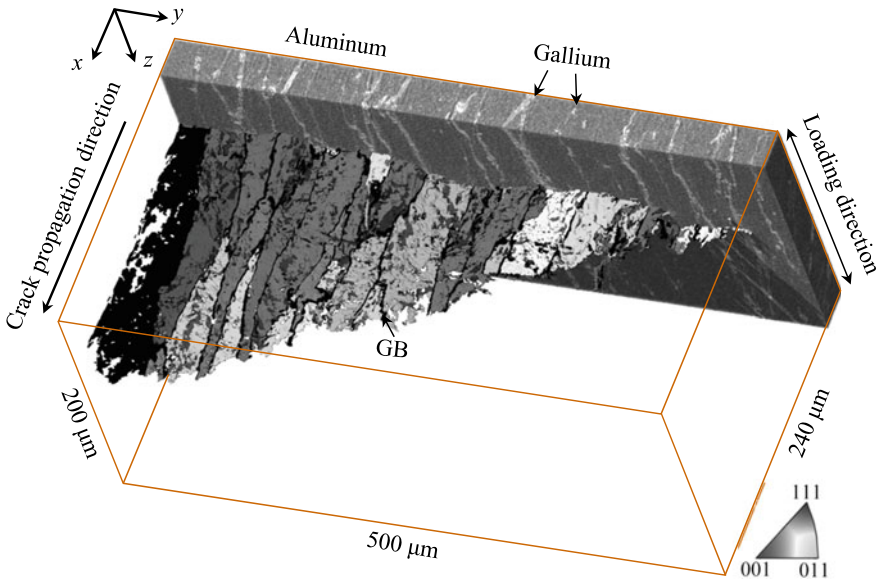

Fig. 6.37 Relationship between fatigue crack propagation and crystallographic structure in an A7075 aluminum alloy [15]; research example that combines 3D imaging of a crystallographic structure using DAGT and continuous observations of crack propagation behavior. The influence of crystallographic structure can be seen in regions where stable crack growth is observed. The original figure is in color; please refer to the figure in the original publication for details

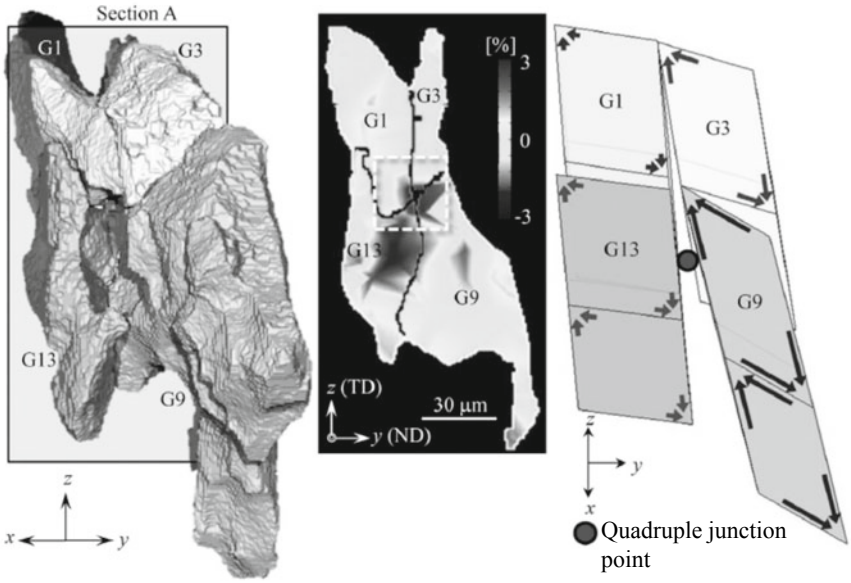

Fig. 6.38 Visualization example of crystallographic grains during tensile deformation using DAGT [16]; 3D display of the four crystallographic grains that surround the grain boundary quadruple point within an Al-3% Cu alloy (left) and a 3D strain mapping shown with a virtual cross-section (see Sect. 9.2.3 for reference). Right: four unit boxes selected from the crystallographic grain where the strains measured by DAGT are applied and where the displacements are emphasized by a factor of 5. The formation of voids due to hydrostatic tension near the grain boundary quadruple point is simulated. The original figure is in color; please refer to the figure in the original publication for details

high crack propagation rate was observed when propagating along a specified crystal orientation.

Figure 6.38 shows an example of DAGT applied to the analysis of damage during tensile deformation [16]. Hydrostatic strain distribution was measured at the quadruple junction point of the grain boundaries. The deformation in the vicinity of the grain boundary was substituted with unit boxes for higher visibility, demonstrating that there was particularly large shear deformation present at crystallographic grain 9 (G9) and the deformations of the other three crystallographic grains were relatively coordinated [15]. The hydrostatic tension generated by this mismatch accelerates void formation and propagation and acts as the cause of macro-scale fracture [15].

6.7 Selection of Devices and Conditions

6.7.1 Device Selection

As observed until now, the spatial resolution of X-ray tomography devices is a little <1 μm at most with projection-type X-ray tomography and is equivalent to a high-spatial-resolution optical microscope. Furthermore, imaging-type X-ray tomography has a spatial resolution that is worse than the scanning electron microscopes, which are widely used for surface observations, by two orders of magnitude. For this reason, it is sometimes the case that internal structures or microstructures close to the effective spatial resolution are observed with X-ray tomography. Furthermore, scanning electron microscopes, optical microscopes, and stereoscopic microscopes have the characteristic of easily being able to change their magnification during observation. Meanwhile, X-ray tomography cannot change its magnification or has serious limitations in doing so. For example, it may appear at first glance that the magnification in a cone-beam CT can be freely changed. However, increasing the magnification and attempting to observe a smaller structure results in the sample protruding out of the field-of-view. In these cases, image quality deterioration is inevitable, unless the specialized image reconstruction techniques as in Sect. 3.3.5 (2) are used. A factor that must be controlled in these instances is the *trade-off between spatial resolution and the field-of-view*. For example, the various X-ray CT scanners summarized in Table 6.1 frequently have a two-dimensional detector with 1000–4000 pixels. As shown with the solid line in Fig. 6.39, the spatial resolution is stipulated by the sample size divided by the pixel number, multiplying this by two, when a device that assures high spatial resolution is used and when the Nyquist frequency based on the sampling theorem discussed in Sect. 7.5.1 (2) constrains the spatial resolution. When the sample size doubles, in this case, the spatial resolution worsens by a factor of two. However, the spatial resolution levels off, as shown in the dotted line in Fig. 6.39 when there are some influences from the X-ray source, sample rotation stage, or detector.

Figure 6.40 shows a schematic of these types of X-ray tomography constraints. Scanning electron microscopes and optical microscopes have a wide range of visualization, so they have many opportunities to favorably conduct observations without any particular considerations. Meanwhile, the chemical composition, density, and size of internal structures/microstructures, which can be visualized, vary according to the performance of the X-ray CT scanner itself, as well as various imaging conditions such as X-ray energy, sample size, and X-ray brilliance.

For these reasons, X-ray tomography does not show much promise as a versatile observation method. First, one must abandon the notion of "the greater also serves for the lesser," instead narrowing down the method to the most important observation subject, determining the optimal X-ray energy, spatial resolution, and imaging techniques based on the fundamental knowledge provided in this book, as well as closely examining the devices, imaging conditions, and samples to be used. Figure 6.41 shows an overview of this process. Conventional surface observation devices were

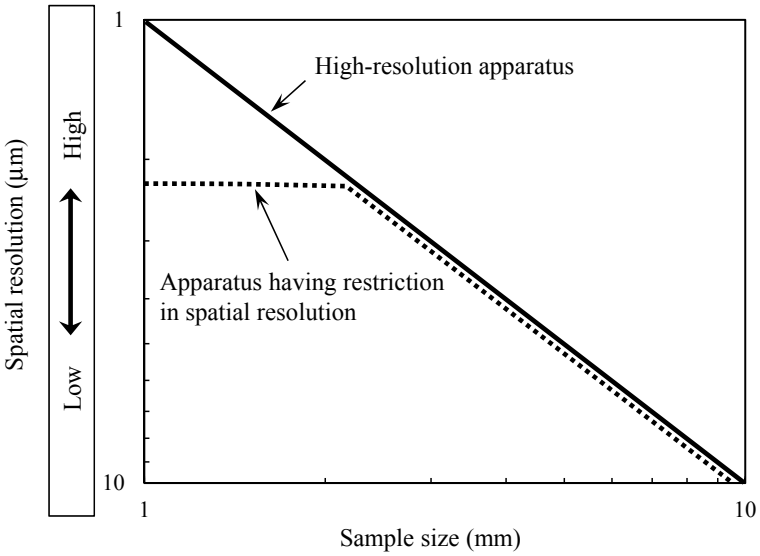

Fig. 6.39 Trade-off between spatial resolution and sample size. Two cases where the spatial resolution is constrained across the entire sample size range due to the Nyquist frequency based on the sampling theorem and where spatial resolution limitations exist due to the device are shown schematically. A detector pixel number of 2000 pixels and a rotation step in the sample rotation stage whose angular increments correspond to this are assumed

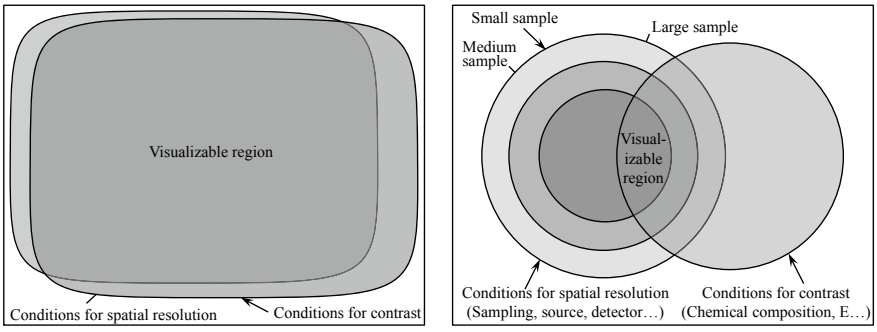

Fig. 6.40 Comparisons between the conventional scientific/engineering observation method of scanning electron microscopy or optical microscopy, as well as X-ray tomography. The rectangular outer frame stipulates the whole. Furthermore, the figures in the frame are constrained by spatial resolution and contrast. The ability to visualize (inside the diagrams) or not visualize (outside the diagrams) is determined based on these conditions. Areas where the diagrams overlap are the regions where the samples are observed in terms of both spatial resolution and contrast. In the case of X-ray tomography in (**b**), the sample size plays a large role in the visualizable range (internal structures, microstructures and their size)

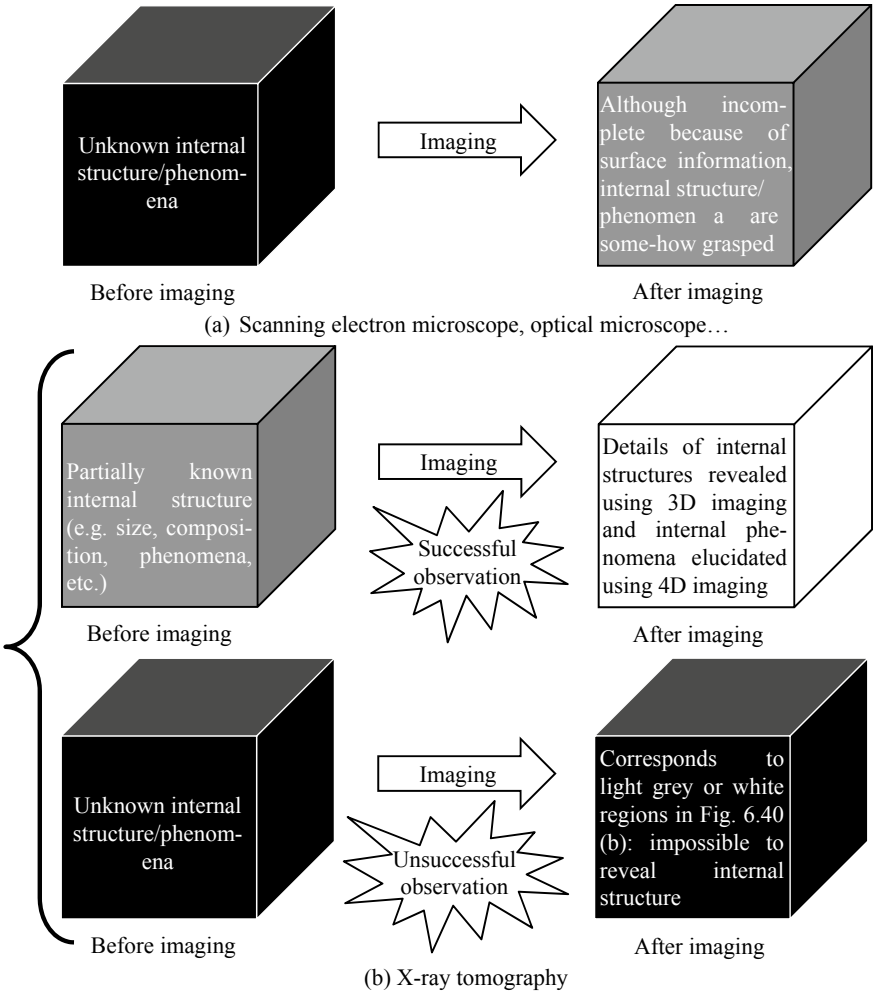

Fig. 6.41 Schematic showing necessary information (black box-gray box) for conventional scientific/engineering observation methods and X-ray tomography prior to observation, and observation results (black box-white box)

expected to transform a black box object into a white box object; in other words, the expectation is that at least some kind of information can be obtained even if the sample is unknown by some form of observation. However, what is actually obtained is only superficial information and assessments are conducted by averaging the observable information as individual structures cannot be assessed. In this sense, the endpoint in Fig. 6.41a is set as a gray box because an accurate determination/understanding of the internal structure or phenomenon cannot be made. By contrast, X-ray tomography is thought to take a gray box sample, where the interior is known to some degree and convert it completely into a white box. Researchers occasionally state,

"there was a sample (black box) that I wanted to observe but couldn't effectively do so." This is oftentimes the case when visualization is technically possible but where results yield no significant findings due to insufficient advance considerations on the sample, actual device, or imaging conditions.

However, discoveries have been made in samples such as in Fig. 6.41a, where the internal structure was previously unknown, leading to significant findings. A representative example of this is the discovery of high-density pores in aluminum reported in Ref. [17]. This occurred when high-density hydrogen micropores with diameters less than 10 μm were coincidentally discovered during synchrotron radiation experiments conducted in 2001 to observe fatigue cracks in aluminum [18]. These types of pores could not be observed with conventional cross-section observations as they were filled with abrasive powder during sample preparation processes like cutting and polishing. There have been many subsequent reports indicating that aluminum alloy strength, fatigue, and high-temperature defects are controlled by these micropores [19], resulting in contributions not only to metal damage/fracture but also to hydrogen embrittlement and stress-corrosion cracking research, as well as new material development.

Until now, the key to observation success in X-ray tomography has been in selecting the "right tool" for the job. However, as presented in this chapter, the functionality of industrial X-ray CT scanners is consistently increasing. Some scanners are equipped with multiple X-ray sources or detectors and devices that can significantly change X-ray energies. That being said, there are limits to the range over, which a single device can cover. Furthermore, industrial X-ray CT scanners are expensive, and it is prohibitively difficult to prepare different devices for each observation subject. We anticipate further active approaches in these cases, such as applications in coordination with the various X-ray CT scanners, which are being introduced among industrial technology centers throughout the country and the usage of synchrotron radiation facility setups. There may be a high barrier to entry with regards to synchrotron radiation facilities for those who have no experience using them. However, many of these facilities can be used for virtually no cost and high-quality and rich information can be obtained with a few hours' worth of experiments, which could otherwise never be obtained with industrial X-ray CT scanners. As the structure and size of the obtained data are the same, there is no need for concern on how to handle the data. Industrial X-ray CT scanner users have experience with 3D imaging and are versed to some extent with 3D image assessment and processing. As such, the barrier to entry for synchrotron radiation facilities is rather low, once accustomed to their particularities.

6.7.2 Realities of 3D Imaging

The discussion below focuses on projection-type X-ray tomography and considers actual X-ray tomography measurements. The factors to first keep in mind with regards to visualizations are as follows:

(1) Is the sample, component, or product observable from a size standpoint?
(2) Can X-rays sufficiently transmit through the sample size?
(3) Is the spatial resolution sufficient for observing the internal structure and microstructure of interest?
(4) Can a sufficient contrast be obtained for observing the internal structure and microstructure of interest?

Spatial resolution is first constrained due to the trade-offs between spatial resolution and the field-of-view (discussed in Sect. 6.7.1) if condition (1) among these is prioritized. However, the possibility exists that condition (3) may not be satisfied due to this aspect. Thus, the first step is to somewhat characterize the internal structure or texture and identify the X-ray CT scanners and imaging conditions (e.g. number of projections) that can satisfy condition (3). This requires a more or less *a priori approach* , such as using stereoscopic microscopes, optical microscopes, or scanning electron microscopes in a supplemental manner, using reference or bibliographic information. Next, assessments using the information learned in Chaps. 2 and 5 and discussed in Chap. 7 are to be conducted to determine whether conditions (2) and (4) can be satisfied. Except for in-line inspections, observations after cutting the sample should be considered a possibility for satisfying condition (1). One of the greatest benefits of X-ray tomography is its ability to conduct internal or external observations without any chemical or physical pre-processing (e.g. sample cutting or polishing). However, instead of unilaterally insisting on this, efforts should be made to cut the sample and stitch a 3D image after multiple scans of each component, accurately determining its internal structure in this manner.

6.7.3 Sample Size and X-Ray Energy Selection

According to Grodzins, the incident X-ray intensity I_0 necessary for transmission image projection when photon noise is predominant is expressed as follows [20]:

$$I_0 wLt < \frac{DBe^{\mu D}}{w(w\mu)^2\left(\frac{\sigma}{\mu}\right)^2} \tag{6.1}$$

Here, the left-hand side of the equation represents the incident photon number, which is obtained by the cross-sectional area wL (w is the pixel size and L is the beam transmission length) of the beam that penetrates the sample multiplied by the exposure time t.

Furthermore, D is the diameter of the cylindrical sample, μ the average linear absorption coefficient, B a constant that depends on the reconstruction algorithm (approximately 2) [20], and σ is the standard deviation of the image signal (i.e. photon noise).

Assuming that the linear absorption coefficient distribution within the sample is homogeneous, the above-mentioned equation has a minimum value when $\mu D = 2$ [20] or $\mu\ D = 2.22$ [21]. Under these conditions, a constant S/N ratio results in minimal exposure time and a constant exposure time results in a maximal S/N ratio. According to Eq. (6.1), this corresponds to a transmissivity I/I_0 of 11–14%. As shown in Eq. (2.10), μ is dependent on λ, so the X-ray energy should be adjusted so that the transmissivity is at this level. For example, X-ray energy of 14–16 keV corresponds to a transmissivity of 11–14% for a pure aluminum sample with a diameter of around 1 mm. Elements like copper, zinc, and iron, which have atomic numbers considerably larger than aluminum, typically comprise several to 10% of aluminum alloys. For this reason, the author typically uses an X-ray energy of 20 keV for imaging aluminum alloys. Furthermore, the optimal μD becomes rather small for cases where detector-based noise has a large influence, requiring a larger transmissivity of approximately 20–30%. Recent simple analyses by Vopálenský have indicated optimal values of $\mu D = 1$ and transmissivity of $I/I_0 = 37\%$ [22]. Although these analyses have been conducted under bold assumptions, we believe they approximate experimental realities.

References

1. H. Fukami, T. Morita, G. Nakamura, Y. Horii, H. Noda, M. Sakai, N. Arakawa, H. Hayashi, K. Yoshida, K. Murakami, Patent publication, X-ray inspection method, X-ray inspection device and X-ray inspection program, application number 2009002814
2. K. Sato, S. Izumi, Patent publication, Computed tomography imaging device and computed tomography imaging method, patent number 3653992
3. Y. Ito (applicant, Yamaha Motor Company), Patent release publication, patent publication 2013-142678, released July 22, 2013
4. H. Toda, M. Takata, T. Ohgaki, M. Kobayashi, T. Kobayashi, K. Uesugi, K. Makii, Y. Aruga, Adv. Eng. Mater. **8**, 459–467 (2006)
5. R. Mizutani, R. Saiga, S. Takekoshi, M. Arai, A. Takeuchi, Y. Suzuki, Microscopy Today **23**(5), 12–17 (2015)
6. H. Toda, K. Uesugi, A. Takeuchi, K. Minami, M. Kobayashi, T. Kobayashi, Appl. Phys. Lett. **89**, 143112 (2006)
7. H. Su, H. Toda, R. Masunaga, K. Shimizu, H. Gao, K. Sasaki, Md.S. Bhuiyan, K. Uesugi, A. Takeuchi, Y. Watanabe, Acta Mater. **159**, 332–343 (2018)
8. H. Toda, A. Takijiri, M. Azuma, S. Yabu, K. Hayashi, D. Seo, M. Kobayashi, K. Hirayama, A. Takeuchi, K. Uesugi, Acta Mater. **126**, 401–412 (2017)
9. H. Toda, D. Seo, Section 3.4, "Fracture behavior analysis in a two-phase steel using phase contrast imaging". Flex. Strong Steel Mater. NTS (2016), 185–198
10. H. Toda, E. Maire, S. Yamauchi, H. Tsuruta, T. Hiramatsu, M. Kobayashi, Acta Mater. **59**, 1995–2008 (2011)
11. H. Toda, T. Nishimura, K. Uesugi, Y. Suzuki, M. Kobayashi, Acta Mater. **58**, 2014–2025 (2010)
12. Q. Zhang, H. Toda, Y. Takami, Y. Suzuki, K. Uesugi, M. Kobayashi, Phil. Mag. **90**, 1853–1871 (2010)
13. M. Kobayashi, H. Toda, A. Takijiri, A. Takeuchi, Y. Suzuki, K. Uesugi, ISIJ Int. **54**, 141–147 (2014)
14. Y. Takeichi, T. Watanabe, Y. Niwa, S. Kitaoka, M. Kimura, Microsc. Microanal. **24**, 484 (2018)

15. H. Li, H. Toda, K. Uesugi, A. Takeuchi, Y. Suzuki, M. Kobayashi, Mater. Trans. **56**, 424–428 (2015)
16. H. Toda, T. Kamiko, Y. Tanabe, M. Kobayashi, D.J. Leclere, K. Uesugi, A. Takeuchi, K. Hirayama, Acta Mater. **107**, 310–324 (2016)
17. H. Toda, T. Hidaka, M. Kobayashi, K. Uesugi, A. Takeuchi, K. Horikawa, Acta Mater. **57**, 2277–2290 (2009)
18. H. Toda, I. Sinclair, J.-Y. Buffière, E. Maire, K.H. Khor, P. Gregson, T. Kobayashi, Acta Mater. **52**, 1305–1317 (2004)
19. H. Toda, T. Inamori, K. Horikawa, K. Uesugi, A. Takeuchi, Y. Suzuki, and M. Kobayashi: Materials Transactions, 54(201), 2195–2201
20. L. Grodzins, Nucl. Instrum. Methods Phys. Res. **206**, 541–545 (1983)
21. W. Graeff, K. Engelke, *Handbook of Synchrotron Radiation*, vol. 4 (Elsevier, Amsterdam, 1991), pp. 361–405
22. M. Vopálenský, D. Vavřik, and I. Kumpová: Proceedings of the 7th Conference on Industrial Computed Tomography, Leuven, Belgium (iCT 2017), (2017), 7 pages
23. H. Toda, M. Kobayashi, T. Kubo, K. Moizumi, D. Sugiyama, Y. Yamamoto, T. Harada, K. Hayashi, Y. Hangai, Y. Murakami, Journal of Japan Institute of Light Metals **63**, 343–349 (2013)